Doppler Radar Observations of Anticyclonic Tornadoes in Cyclonically Rotating, Right-Moving Supercells

HOWARD B. BLUESTEIN

School of Meteorology, University of Oklahoma, Norman, Oklahoma

MICHAEL M. FRENCH

School of Marine and Atmospheric Sciences, Stony Brook University, Stony Brook, New York

JEFFREY C. SNYDER

Cooperative Institute for Mesoscale Meteorological Studies, University of Oklahoma, and NOAA/OAR National Severe Storms Laboratory, Norman, Oklahoma

JANA B. HOUSER

Department of Geography, Ohio University, Athens, Ohio

ABSTRACT

Supercells dominated by mesocyclones, which tend to propagate to the right of the tropospheric pressure-weighted mean wind, on rare occasions produce anticyclonic tornadoes at the trailing end of the rear-flank gust front. More frequently, mesoanticyclones are found at this location, most of which do not spawn any tornadoes. In this paper, four cases are discussed in which the formation of anticyclonic tornadoes was documented in the plains by mobile or fixed-site Doppler radars. These brief case studies include the analysis of Doppler radar data for tornadoes at the following dates and locations: 1) 24 April 2006, near El Reno, Oklahoma; 2) 23 May 2008, near Ellis, Kansas; 3) 18 March 2012, near Willow, Oklahoma; and 4) 31 May 2013, near El Reno, Oklahoma. Three of these tornadoes were also documented photographically. In all of these cases, a strong mesocyclone (i.e., vortex signature characterized by azimuthal shear in excess of $\sim 5 \times 10^{-3} \, \mathrm{s}^{-1}$ or a $20 \, \mathrm{m \, s}^{-1}$ change in Doppler velocity over 5 km) or tornado was observed $\sim 10 \, \mathrm{km}$ away from the anticyclonic tornado. In three of these cases, the evolution of the tornadic vortex signature in time and height is described. Other features common to all cases are noted and possible mechanisms for anticyclonic tornadogenesis are identified. In addition, a set of estimated environmental parameters for these and other similar cases are discussed.

1. Introduction

It well known that most supercells are dominated in the midtroposphere by storm-scale, cyclonically rotating vortices—mesocyclones—which sometimes spawn cyclonically rotating tornadoes [see Bluestein (2013) and other references within] and that propagate to the right of both the pressure-weighted mean tropospheric wind

and vertical shear vector (we hereafter refer to these as cyclonic supercells). Much more rarely, supercells are dominated by anticyclonically rotating vortices—mesoanticyclones—which dynamically promote propagation to the left of both the pressure-weighted mean tropospheric wind and vertical shear vector, appearing and behaving like mirror images of the mesocyclone-dominated supercells (e.g., Nielsen-Gammon and Read 1995; Knupp and Cotton 1982). On extremely rare occasions, such supercells have been found to produce anticyclonically rotating tornadoes (Monteverdi et al. 2001; Bunkers and Stoppkotte 2007; Bluestein 2013). It is also well understood that the source of vorticity in the

Corresponding author address: Howard B. Bluestein, School of Meteorology, University of Oklahoma, 120 David L. Boren Blvd., Suite 5900, Norman, OK 73072.
E-mail: hblue@ou.edu

TABLE 1. Cases of anticyclonic–cyclonic tornado pairs[a] in supercells.

Date	Location[b]	Reference
13 Jun 1976	Luther, IA	Brown and Knupp (1980)
3 Jun 1980	Grand Island, NE	Fujita (1981)
29 May 2004	Calumet, OK	Bluestein et al. (2007b)
24 Apr 2006	El Reno, OK	Snyder et al. (2007)
23 May 2008	Ellis, KS	French (2012)
29 May 2008	Glen Elder, KS	Wurman and Kosiba (2013)
18 Mar 2012	Willow/Mangum, OK	Current study is the first citation
31 May 2013	El Reno, OK	Wurman et al. (2014), Bluestein et al. (2015)
4 Jun 2015	Simla, CO	Schiller (2015)

[a] But not necessarily at the same time.
[b] At or near the specified location.

parent mesocyclones and mesoanticyclones in the mid-troposphere is horizontal vorticity associated with environmental vertical shear (Rotunno and Klemp 1985) that is tilted onto the vertical by horizontal gradients in vertical motion. However, the primary source of vorticity in *low-level* mesocyclones is thought to be baroclinic generation in the forward-flank region (e.g., Klemp and Rotunno 1983). The source of vorticity of cyclonic tornadoes in supercells is assumed to be the low-level mesocyclone, perhaps enhanced through interaction with the rear-flank downdraft [summarized in Bluestein (2013)] and then modified by frictional processes (e.g., Rotunno 2013).

Anticyclonically rotating tornadoes have also been documented in cyclonic supercells at the rear/trailing end (with respect to storm motion) of the rear-flank gust front (RFGF), in tandem with either strong mesocyclones or cyclonic tornadoes (Brown and Knupp 1980; Fujita 1981; Bluestein et al. 2007b; Snyder et at. 2007; Wurman and Kosiba 2013; Wurman et al. 2014; Bluestein et al. 2015). Storm chasers and storm spotters usually focus their attention on the wall cloud, mesocyclone region, or the tip of the leading edge of the RFGF as it cyclonically wraps around the mesocyclone in right-moving supercells, for signs of tornado formation. Complete focus on this region can lead to inattention to early signs of the formation of anticyclonic tornadoes at the other end of the RFGF. For this reason, and because anticyclonic tornadoes in cyclonic supercells are so rare and are usually relatively weak and short lived, warning the public of these anticyclonic tornadoes is much more difficult than warning them of cyclonic tornadoes.

Anticyclonic hook echoes or appendages have been documented in many right-moving supercells (Markowski 2002). Some anticyclonic hook echoes or appendages are found along the trailing edge of the RFGF near where anticyclonic tornadoes form, while others have been documented on the left flank of the storm (Fujita 1963, his Fig. 14; Lemon 1976, his Fig. 1) and as part of the "Owl Horn" radar signature in developing supercells (Kramar

et al. 2005, their Fig. 3). Short-track "satellite" (Edwards 2014) anticyclonic tornadoes have also been documented (e.g., Tanamachi et al. 2012) in supercells with cyclonic tornadoes, but these are not the focus of this study; the satellite tornadoes, unlike the other anticyclonic tornadoes that are the focus of this study, were transient and rotated around the main, cyclonic tornado. Anticyclonic tornadoes have also been documented in ordinary-cell convective storms (Kosiba et al. 2014). If the source of vorticity in cyclonic tornadoes in supercells is that of the low-level mesocyclone, then an important scientific question is the following: What is the source of vorticity for anticyclonic tornadoes in cyclonically rotating supercells and how does anticyclonic tornadogenesis proceed? It is suspected that anticyclonic tornadogenesis in cyclonic supercells is not simply the mirror image of cyclonic tornadogenesis in cyclonic supercells owing to the lack of symmetry on the storm-scale in supercell structure.

It is thought that similar-appearing couplets of vorticity in quasi-linear convective systems (QLCSs) are created by the tilting of horizontal vortex lines by rising motion or sinking motion at the center of the lines (Weisman and Davis 1998) (hypothesis 1). In the case of a supercell, the source of horizontal vorticity could similarly be (hypothesis 1a) baroclinic generation along the leading edge of the RFGF if the air to its rear is relatively cold, or (hypothesis 1b) environmental vorticity associated with vertical shear. A jetlike feature in the rear-flank downdraft straddled by a cyclonic–anticyclonic couplet of vorticity may be similar to the rear-inflow jet in an MCS/QLCS (Weisman 1992, 1993). However, since supercells are highly three dimensional, other mechanisms may create the jet, such as dynamic vertical perturbation pressure gradients (e.g., Skinner et al. 2014) due to the decrease of vorticity with height, or to localized generation of negative buoyancy due to evaporation, sublimation, or melting. The actual production of the anticyclonic–cyclonic couplet in vorticity is due to the tilting of horizontal vorticity, but the source of the horizontal vorticity is not known precisely.

TABLE 2. Selected comparative characteristics of the radars.

Name	Wavelength	Half-power beamwidth	Range gate depth	Platform	Cases
MWR-05XP	3 cm	1.8° azimuth/2° elevation	150 m	Truck	23 May 2008
RaXPol	3 cm	1°[a]	30–75 m	Truck	18 Mar 2012
					31 May 2013
TDWR	5 cm	0.5°	150 m	Fixed site	24 Apr 2006
					31 May 2013

[a] The effective azimuthal beamwidth due to beam smearing is 1.4°. This beam smearing may be eliminated using the "strobe technique." For the data collected by RaXPol for the storms listed in Table 1, the strobe technique was not implemented because raw I/Q data were not recorded (Pazmany et al. 2013).

Markowski and Richardson (2014), in highly idealized numerical experiments of simulated supercells, examined the origin of anticyclonic vortices along the trailing end of the RFGF opposite that of the mesocyclone and found that the (hypothesis 1a) strongest anticyclonic vortices were produced when the "heat sink," a measure of the evaporative cooling in the forward flank of the supercell, was relatively weak and the low-level environmental vertical shear high. In this case, however, the mesocyclone was relatively weak, which is not what was found in some of the cases documented herein. If the source of vorticity in anticyclonic tornadoes from right-moving supercells is the anticyclonic vorticity produced at the end of the RFGF, then why do some mesoanticyclones produce tornadoes, while others do not? This is the same question asked about cyclonic tornadoes and the motivation for recent field experiments (e.g., Wurman et al. 2012), except for mesoanticyclones and a question to which we also do not yet have a definitive answer.

It is also possible that the source of vorticity in the anticyclonic tornadoes is not from a parent meso-anticyclone (produced via tilting), but rather from (hypothesis 2) preexisting anticyclonic shear vorticity on the anticyclonic-shear side of the low-level jet associated with the rear-flank downdraft, behind the RFGF or in a secondary surge. In this case, the concentration of vorticity (hypothesis 2a) might be a result of lateral shear instability and stretching associated with growing updrafts along the flanking line. Such a mechanism of tornadogenesis might be similar to that in "landspouts" or nonmesocyclone tornadoes in ordinary cell convection (e.g., Bluestein 1985; Wakimoto and Wilson 1989; Lee and Wilhelmson 1997).

The main objectives of this paper are to present more detailed documentation of anticyclonic tornadoes in cyclonic supercells and to seek qualitative observational evidence for how these anticyclonic tornadoes may form. The decades-old case studies described in the refereed literature lack storm-scale and substorm-scale detail because they made use only of analog, radar-reflectivity data and fixed-site surface observations (Brown and Knupp 1980; Fujita 1981; Fujita and Wakimoto 1982); more recently, a case study made use of polarimetric, Doppler radar data, but it was collected only at one elevation angle (Bluestein et al. 2007b; Much more recently, anticyclonic tornadoes in cyclonic supercells have been documented volumetrically as a function of time by Doppler radars, some with rapid-scan capability, and some both polarimetric and rapid-scan capability. The cases that are discussed in this study occurred near El Reno, Oklahoma, on 24 April 2006 (Snyder et al. 2007); Ellis, Kansas, on 23 May 2008 (French 2012); Willow, Oklahoma, on 18 March 2012; and El Reno on 31 May 2013 (Wurman et al. 2014; Bluestein et al. 2015). Although these cases were selected because they were readily available to the authors, they are not an exhaustive set of what is actually available. A list of all documented cases known to the authors is found in Table 1.[1]

The data sources and methodologies of data processing for the Doppler radar data are described in section 2. The four cases of anticyclonic tornadoes in cyclonically rotating, right-moving supercells are discussed in section 3. A summary of our findings and speculation about how anticyclonic tornadoes form in cyclonic supercells are found in section 4.

2. Data

The primary data used in this study came from two different mobile, X-band (~3-cm wavelength), rapid-scan, Doppler radars: the Mobile Weather Radar, 2005 X-band, Phased Array (MWR-05XP; Bluestein et al. 2010) and the Rapid scanning, X-band, Polarimetric (RaXPol; Pazmany et al. 2013). Data from a nearby Terminal Doppler Weather Radar (TDWR; Vasiloff 2001), TOKC (in the northwest section of Norman,

---

[1] Of the nine cases listed in Table 1, two occurred near El Reno, OK, and one occurred in Calumet, OK, which is ~15 km from El Reno. It is not thought that any topographic feature is responsible for this apparent statistical anomaly, but rather it is likely due to the proximity to the more frequent radar deployments in this area owing to the relative ease in getting to this area from the authors' home institution.
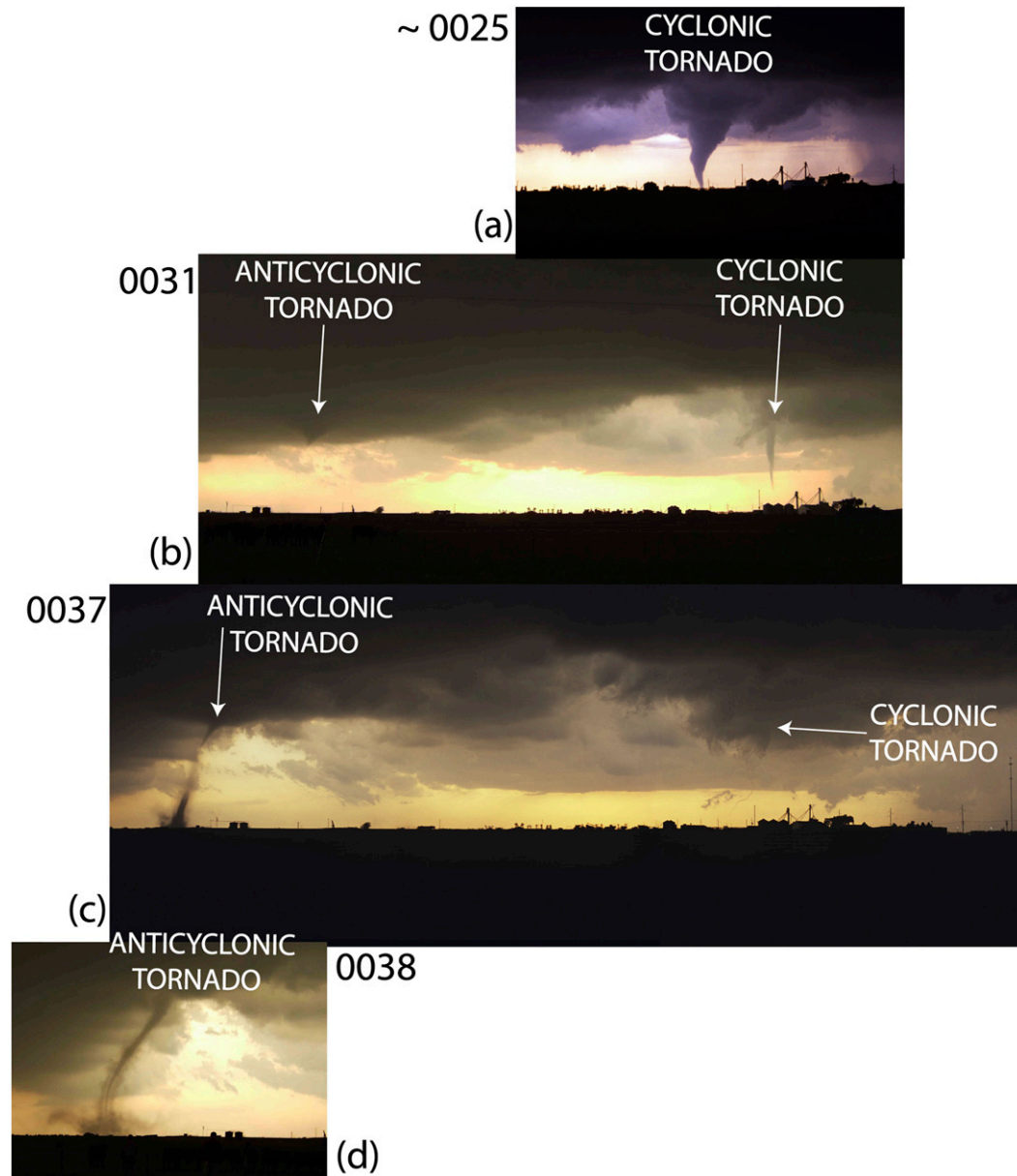
FIG. 1. Photographs of tornadoes just south of El Reno, OK, on 25 Apr 2006 at the times in UTC indicated (local time is 5 h earlier, on 24 Apr). View is to the west from a location ~0.5 km south of I-40 on Highway 81. (a) Cyclonic tornado at ~0025 UTC, (b) dissipating cyclonic tornado and clear slot (right arrow) and funnel cloud of developing anticyclonic tornado (left arrow) at 0031 UTC, (c) remnant of funnel cloud of cyclonic tornado (right arrow) and anticyclonic tornado (left arrow) at 0037 UTC, and (d) mature anticyclonic tornado at 0038 UTC. The photographs were taken ~3–3.5 mi (~5–5.5 km) from the anticyclonic tornado and ~6–7 mi (9.5–11 km) from the cyclonic tornado. (Photographs courtesy of H. Bluestein.)

Oklahoma, south of Oklahoma City), were also used when mobile Doppler radar data were not available. A summary of the primary characteristics of all three radars is given in Table 2.

The intensity of vertical vortices within supercells was measured from vortex signatures (VSs) and tornadic vortex signatures (TVSs). A discussion of the criteria used herein to define a TVS and how it differs from a vortex signature (VS) is given in French et al. (2013). In brief, gate-to-gate azimuthal shear represented by ΔV, the largest magnitude difference between the local maximum and minimum Doppler velocities in the shear signature, must be $\geq 20\,\mathrm{m\,s^{-1}}$ and the distance between the local maximum and minimum in range or azimuth

is ≤2 km. These criteria are similar to those used by others (Trapp et al. 1999; Alexander 2010; Kosiba et al. 2013) based on data from different fixed-site and mobile radars but modified to account for the different resolution (Wood and Brown 1997) of the MWR-05XP, TDWR, and RaXPol and to match times and locations given in damage surveys when possible. The criteria used, however, do not necessarily indicate that there actually was a tornado (French et al. 2013; Houser et al. 2015), but instead were chosen as an objective measure of vortex intensity based on single-Doppler radar data and are especially useful in documenting tornado track and relative intensity when damage-survey data are not available. In summary, the threshold ΔV separating a VS from a TVS is radar and range dependent, and may vary from 20 to as much as $40 \, \mathrm{m \, s^{-1}}$.

The MWR-05XP is a hybrid, phased-array (electronically scanning in elevation angle) and mechanically scanning (in azimuth) mobile radar.[2] Details on how it has been used to study the evolution of the parent vortices of tornadoes are found in French et al. (2013) and French et al. (2014). The main strength of the MWR-05XP is the relatively short time it takes to scan a sector volume (5–20 s, depending on the year it was used as its capabilities have evolved over the years, how many elevation angles are scanned, and the angular width of the sector volume). The main weaknesses of the radar are its relatively coarse spatial resolution owing to its half-power beamwidth of 1.8° [cf. ~1° for other mobile, X-band radars; e.g., the Doppler on Wheels (DOW) and the University of Massachusetts X-Pol, cf. Wurman et al. (1997); Tanamachi et al. (2012)] and that, prior to 2015, it did not have leveling capability, so great care was taken to deploy it on roads that appeared to be level, but the exact elevation offset was unknown. These two weaknesses limit the usefulness of the radar to storms at relatively close range (within ~20-km range, where azimuthal resolutions of ~600 m or better are attained) and knowledge of the height of the vortex signatures (an error of 3° could yield an error of ~1 km at a range of 20 km). In addition, the interpretation of vortex signatures at constant elevation angle must take into account differences in the height of the radar beam across the vortices; for example, at 1° elevation angle, the difference in height across a Doppler velocity couplet 5 km in diameter at 20-km range is ~90 m. However, for the purpose of locating regions of coherent Doppler velocity vortex signatures associated with the parent mesocyclone

---

[2] After 2008, electronic back scanning to increase the dwell time in radar volumes was implemented, but this is not relevant to this study, which makes use of data only from 2008.
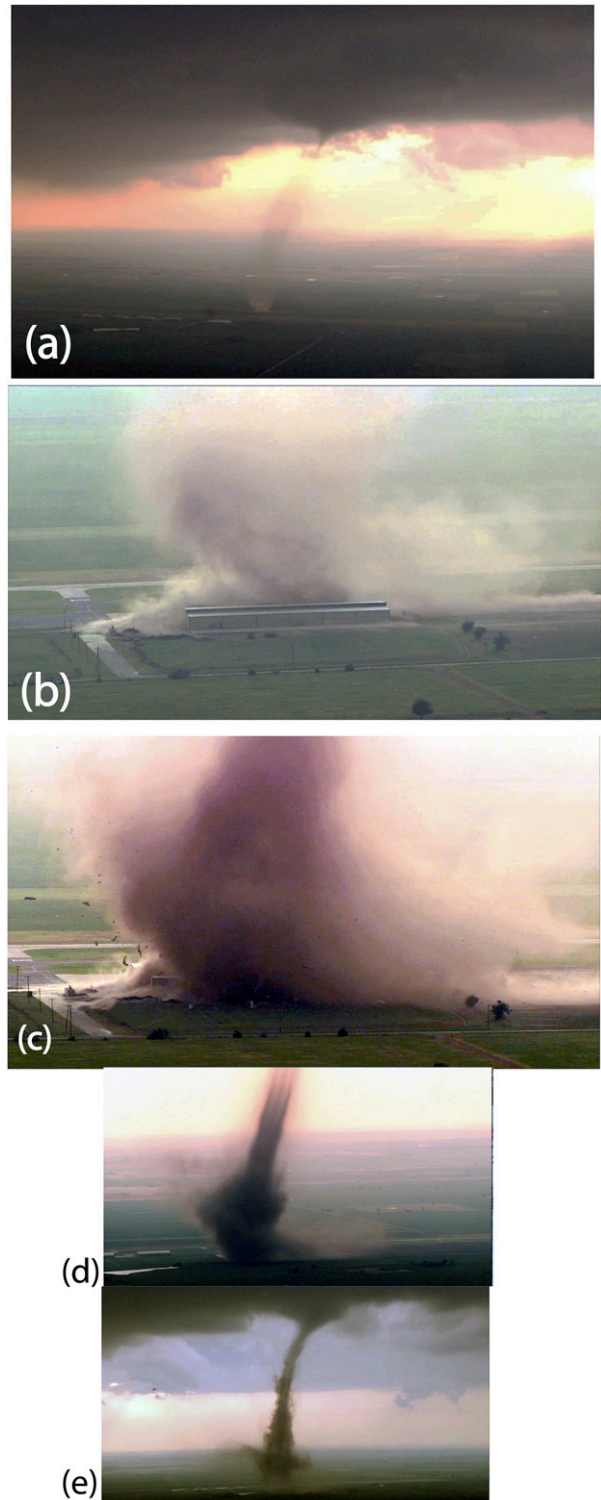

FIG. 2. Frame captures from a video of the anticyclonic tornado just south of El Reno, OK, on 24 Apr 2006, as taken from the KWTV Oklahoma City helicopter by M. Dunn (courtesy of G. England), looking to the west/west-southwest. (a) Beginning of the tornado (after Fig. 1b, but before Fig. 1c); (b) close-up view of the tornado as it is hitting the El Reno Regional Airport; (c) as in (b), but when the tornado is damaging the hangar at the airport; (d) the mature stage of the tornado (cf. Fig. 1d); and (e) the dissipating stage of the tornado.
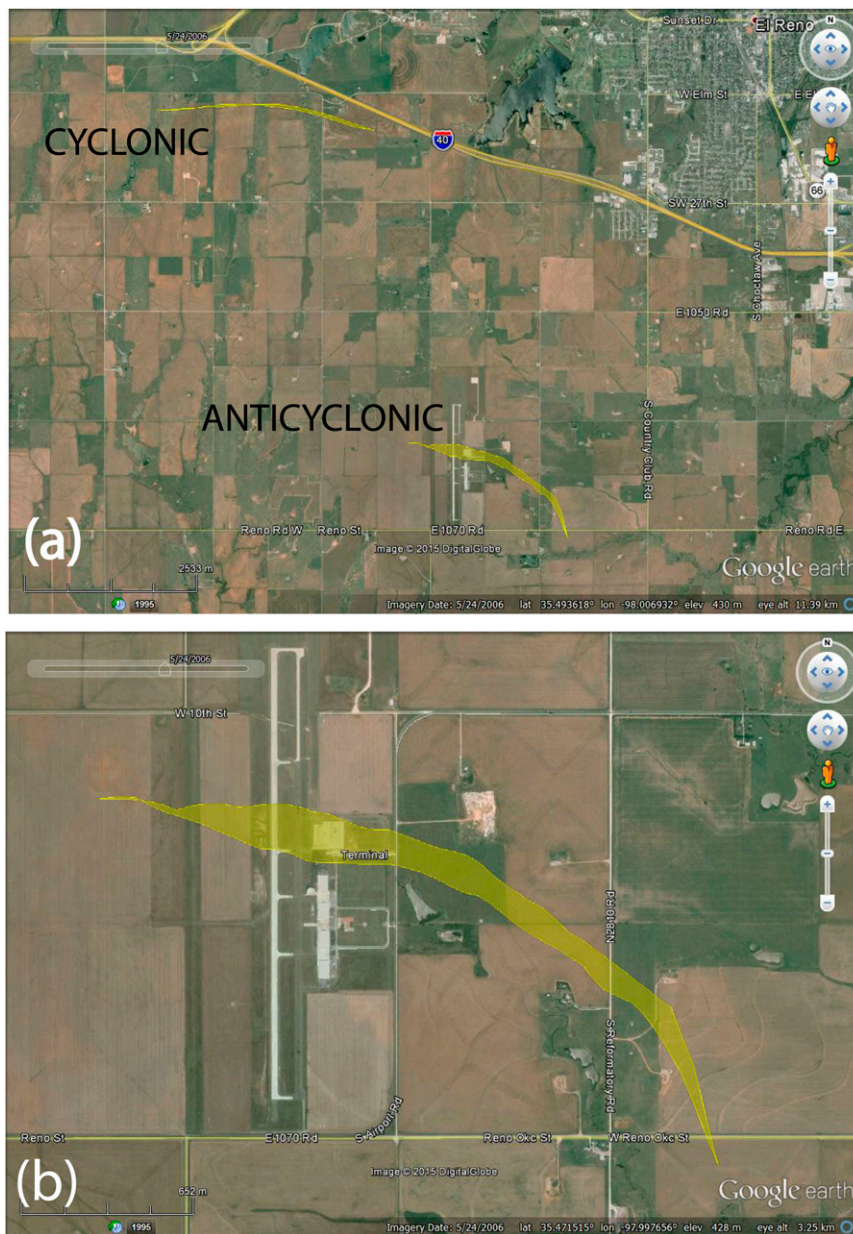
FIG. 3. (a) Broad view of the damage tracks (courtesy of the National Weather Service Forecast Office in Norman, OK) of the cyclonic (northernmost track) and anticyclonic (southernmost track) tornadoes near El Reno on 24 Apr 2006, and (b) close-up view of the damage track of the anticyclonic tornado; the El Reno Regional Airport is at the leftmost section of the damage track. Square sections are 1 mi (1.6 km) along each side. (Courtesy of G. Stumpf, Cooperative Institute for Mesoscale Meteorological Studies, University of Oklahoma.)

of tornadoes within ~20-km range, for estimating vorticity qualitatively via the azimuthal shear of the Doppler velocity, and to determine if a vortex signature propagates vertically, it has been found to be very useful (French et al. 2013, 2014).

RaXPol is a mechanically scanning, polarimetric, mobile Doppler radar that can scan much more quickly than most polarimetric, X-band radars because a high-speed pedestal is used and frequency hopping is employed to increase the number of independent samples: the azimuthal scanning rate can be as fast as $180° s^{-1}$ (Pazmany et al. 2013). Thus, it takes ~20 s to collect a full volume consisting of 10 elevation angles. Although its beamwidth is narrower than that of the
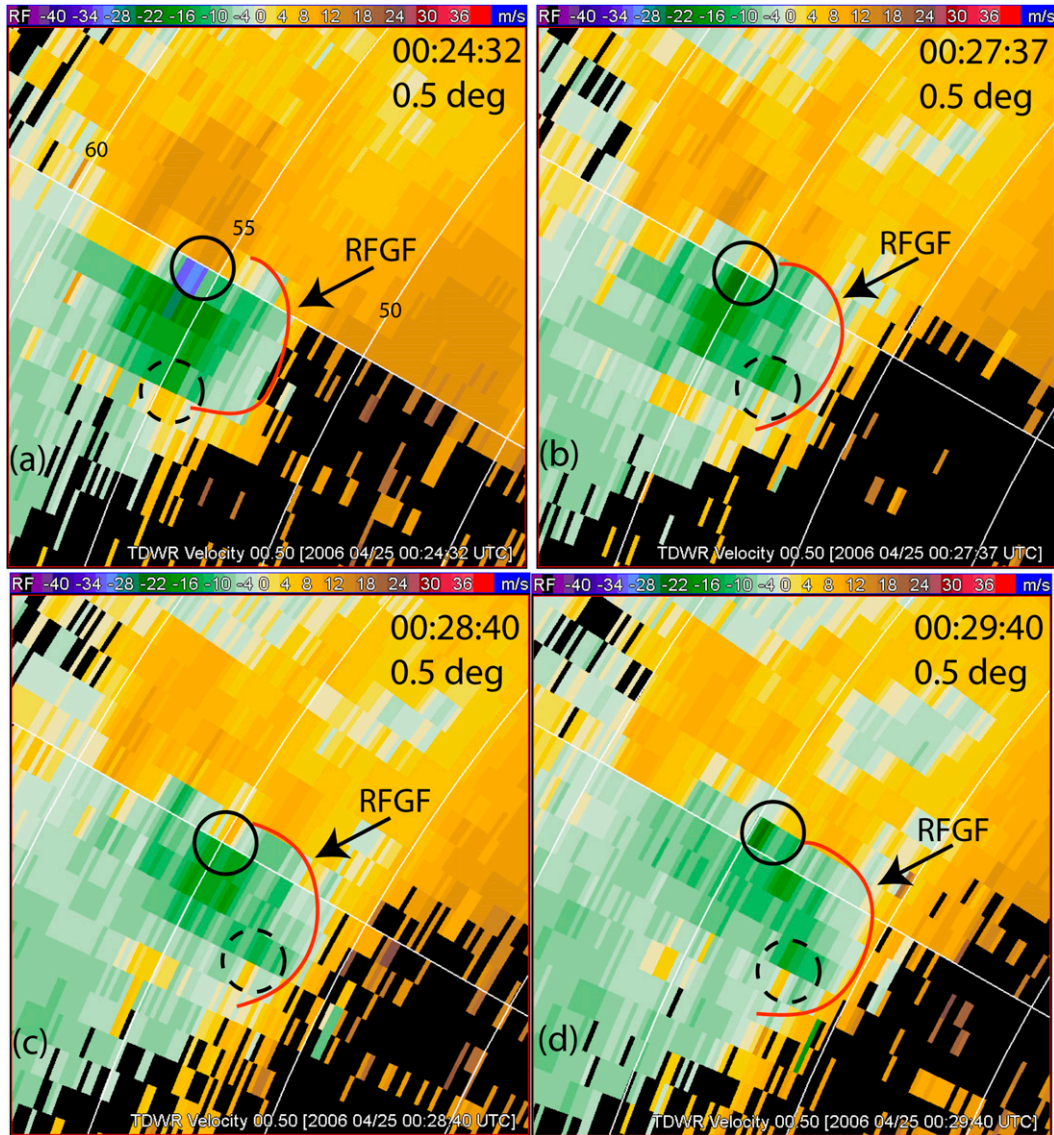
FIG. 4. The dissipation of the cyclonic tornado and formation of the anticyclonic tornado near El Reno, OK, on 24 Apr 2006 as depicted by TOKC TDWR Doppler velocity data (m s^{-1}, color scale at the top of each panel) at low altitude, ~450 m ARL [0.5° elevation angle plan position indicators (PPIs)]. Times are shown on 25 Apr 2006: (a) 0024:32, (b) 0027:37, (c) 0028:40, and (d) 0029:40 UTC. The solid (dashed) black circles mark the locations of the cyclonic-shear (anticyclonic shear) signatures/TVSs; the curved red line marks the approximate location of the leading edge of the RFGF determined from the 0 m s^{-1} isodop. North is in the 360° direction. Range rings are plotted in km.

MWR-05XP, its effective beamwidth is only slightly narrower (~1.4°–1.5°), owing to beam smearing resulting from the rapid mechanical scanning [Doviak and Zrnić (1993), their Eq. (7.34); Bluestein et al. (2015)]. Overall, its volumetric update time is longer than that of the MWR-05XP but RaXPol's azimuthal and elevation angle resolution are finer, it has polarimetric capability, and it most often collects data from a full 360° in azimuth.

RaXPol provides the polarimetric variables differential reflectivity Z_{DR} and copolar cross-correlation coefficient ρ_{hv}, among others. These variables can be useful in identifying the type of scatterers in the radar volume; in particular, they can be used to distinguish between debris (typically $Z_{DR} < 0.5$ dB and $\rho_{hv} < 0.80$) and precipitation (typically $Z_{DR} > 1$ dB and $\rho_{hv} > 0.90$) near and within tornadoes (e.g., Ryzhkov et al. 2005; Bluestein et al. 2007b; Snyder et al. 2010; Schultz et al.
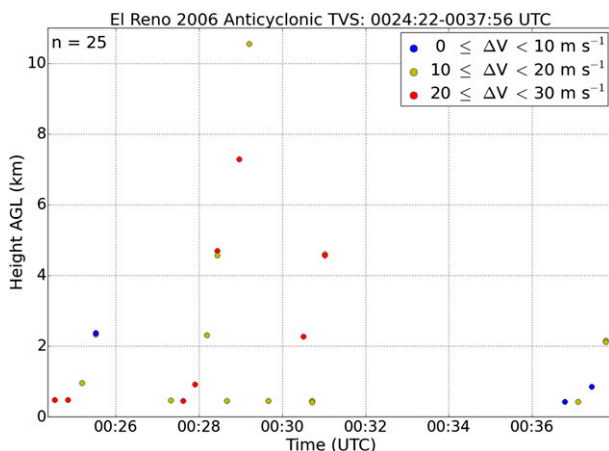
FIG. 5. The formation of the anticyclonic tornado near El Reno, OK, on 26 Apr 2006 as depicted by a measure of the gate-to-gate shear (ΔV) as a function of time (UTC on 25 Apr) and height AGL (km). A total of 25 (*n*) measurements were made. Based on TOKC TDWR data. No data were available for analysis during 0031–0036 UTC.

2012; Bodine et al. 2013; Snyder and Bluestein 2014; Wurman et al. 2014; Snyder and Ryzhkov 2015). In this study, polarimetric data were used mainly to identify tornado debris.

The mobile Doppler radar velocities were both automatically and manually dealiased depending on the difficulty of doing so and displayed using Solo II (Oye et al. 1995) or Solo 3. Data were otherwise edited as described by French et al. (2013) and Bluestein et al. (2015).

TDWR data only were used for one case (24 April 2006) because it was the closest radar to the storm being studied and no mobile radar data were available. TDWR data supplemented the mobile-radar data used in another case (31 May 2013) because the mobile radar was in motion during the genesis of the anticyclonic tornado, so the mobile radar dataset did not capture tornadogenesis. The TDWR (Vasiloff 2001) operates at C band (~5-cm wavelength) and has a half-power beamwidth of 0.5°. Compared to the X-band mobile radars, it is useful out to longer ranges because it suffers less from attenuation in the presence of heavy precipitation and has a much narrower beam. The scanning strategies are more complicated and less consistent (i.e., they do not sample in time or space uniformly) than those used by the WSR-88Ds (Crum and Alberty 1993).

Photographs taken from the site of the mobile radar were used when appropriate (18 March 2012 and 31 May 2013), as were photographs taken for one case when mobile radar data were not available (24 April 2006). For one case photographic documentation was not available (23 May 2008) because this case was at night.

Photographic documentation has been used in conjunction with mobile Doppler radar data to correlate cloud features with radar-observed features (e.g., Wakimoto and Martner 1992; Bluestein et al. 2007a; Wakimoto et al. 2011, 2012, 2015). There is an uncertainty of as much as 2 min in the clock time of some of the photographs used in this study because at the end of the storm seasons, the camera clock deviated from the actual time by as much as 2 min, as it was not recalibrated prior to each deployment. For storm motion ~$O(10)$ m s^{-1}, there could, therefore, be an error of ~1 km in the location of features in the photographs with respect to the Doppler radar features, though much care was taken to correct the clock times as much as possible. Thus, some caution must be exercised when comparing visual to radar-observed features.

Data from a number of model analysis systems—for example, the Rapid Update Cycle (RUC), RUC2, Rapid Refresh (RAP), and NCEP's North American Regional Reanalysis (NARR; Brown et al. 2011)—were used to construct estimated proximity soundings for most of the cases presented, as done by Markowski et al. (2003) for similar purposes using only RUC data, since operational or special soundings were not available near most of the storms.

3. Selected cases

a. 24 April 2006

A supercell near El Reno, Oklahoma, produced a cyclonic tornado [rated as low-end F1 on the Fujita scale; Fujita (1981)] late in the afternoon of 24 April 2006 (Fig. 1a). As the condensation funnel associated with the cyclonic tornado narrowed, a funnel cloud appeared to its south along the far southern end of a curved cloud base (Fig. 1b), which appeared visually to be (and verified later on in this paper on the basis of radar data) located near the leading edge of the RFGF. The narrowing of the funnel cloud associated with the cyclonic tornado ("shrinking stage") was associated with the dissipation of the tornado (Golden and Purcell 1978). A debris column then appeared underneath the new funnel cloud (Figs. 1c and 2a) after the funnel cloud associated with the cyclonic tornado had almost completely disappeared. The condensation funnel pendant from the cloud base above and the surface debris cloud then became connected to each other (Fig. 1d) as the cyclonic tornado completely dissipated. The formation of this second tornado, to the south of the original tornado, caught the authors present at the storm off guard because attention was focused on the cyclonic tornado, not on the southern end of the curved cloud base/RFGF. It
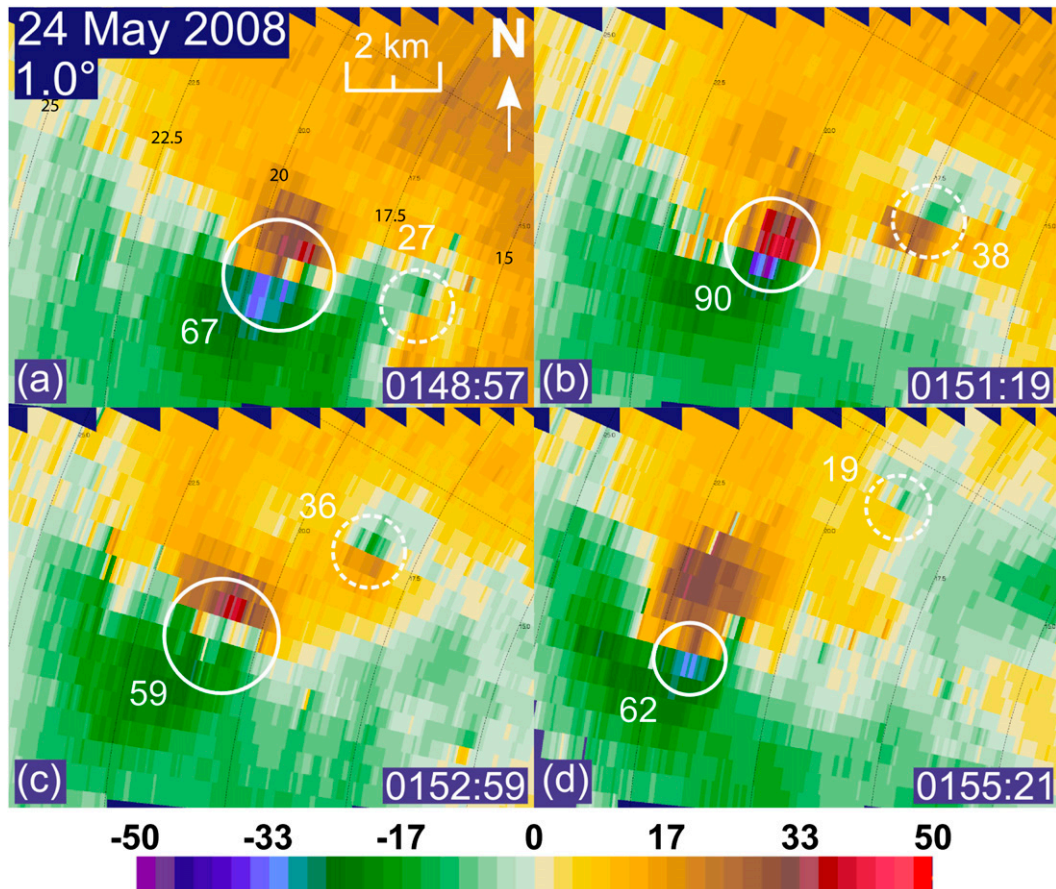
FIG. 6. Rotation of anticyclonic vortex signature (white dashed circle) about a cyclonic tornadic vortex signature (white solid circle) on 23 May 2008 for the Ellis, KS, supercell. Doppler velocity from the MWR-05XP at 1° elevation angle (color scale in m s^{-1}) at (a) 0148:57, (b) 0151:19, (c) 0152:59, and (d) 0155:21 UTC 24 May. The maximum ΔV in m s^{-1} is indicated next to each vortex signature/TVS. The approximate center beam height at the location of the anticyclonic vortex signatures are (a) 280, (b) 300, (c) 320, and (d) 330 m AGL. North is in the 360° direction. Range rings are shown every 2.5 km.

is, therefore, important for spotters to be aware of the possibility of (anticyclonic) tornadoes forming to the south of existing (cyclonic) tornadoes, at the southern end of a RFGF.

From close-up video of the southern tornado taken from a television helicopter (which was widely disseminated and viewed at the time), it can be seen that this tornado (rated high-end F1 on the Fujita scale) was rotating anticyclonically (Fig. 2b); debris was seen rising helically in the tornado in a clockwise manner, while part of the debris column was leaning to the left (south) with height as seen in Fig. 2b. At the time of the frame capture shown in Fig. 2b, the tornado was over El Reno Regional Airport and about to hit a hangar. As the tornado debris cloud completely enveloped the hangar, some individual pieces of debris were observed ejecting radially outward on the left (south) side of the hangar (Fig. 2c). The tornado then took on the appearance of an

inner, narrow condensation funnel and an outer debris cloud or condensation funnel (Fig. 2d; e.g., Bluestein 2013, Fig. 6.56). It leaned to the right (i.e., had a component of tilt to the north with height) (Figs. 1d and 2d) and then began to dissipate, as wavelike disturbances appeared to propagate vertically along the edges of the funnel (Fig. 2e).

The damage tracks of the cyclonic and anticyclonic tornadoes were quasi parallel, but the anticyclonic tornado's damage track was curved more to the south at its termination region (bottom track in Fig. 3a). This behavior is a mirror image of what frequently occurs during the decay of cyclonic tornadoes [which often curve to the left during decay depending on their location with respect to a parent cyclone; Agee et al. (1976)] and may be consistent with the component of tilt toward the north with height seen in the photographic documentation later in the life of the anticyclonic tornado
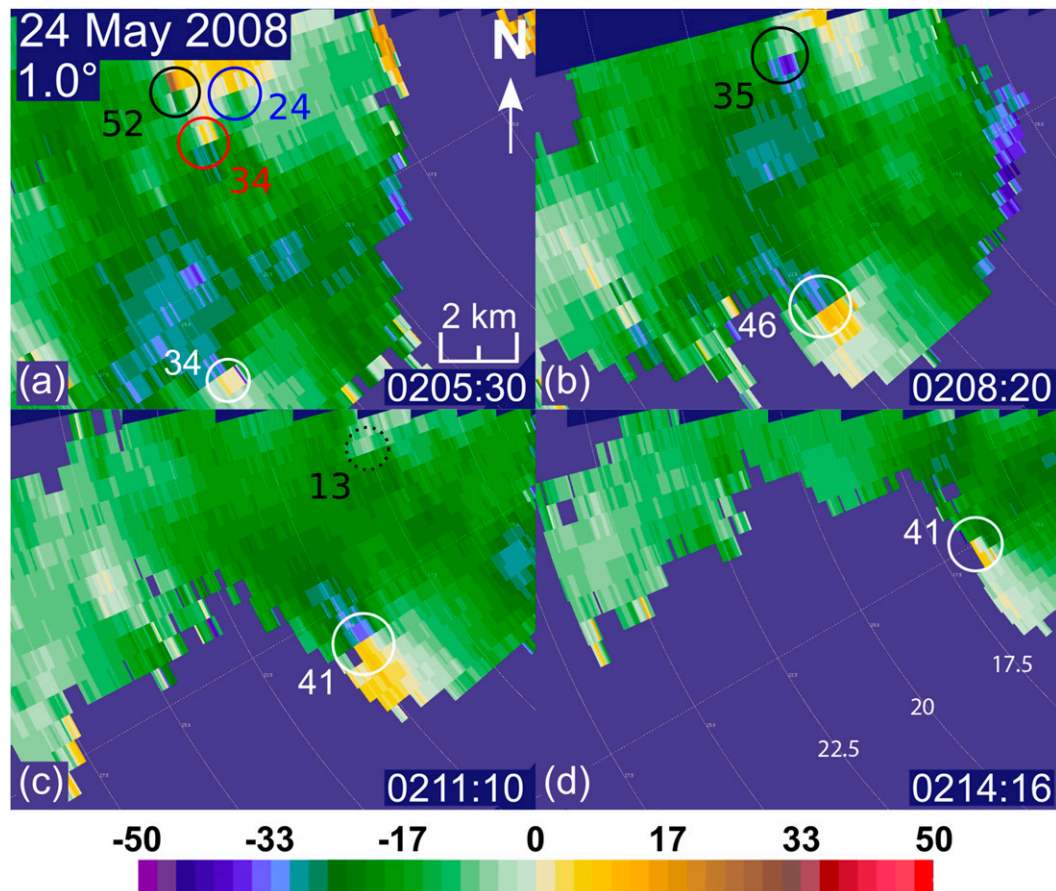
Fig. 7. The behavior of the cyclonic mesocyclone/tornado and mesoanticyclone/tornado in the later Ellis, KS, supercell on 23 May 2008. Doppler velocity from the MWR-05XP at 1° elevation angle at the times indicated in UTC on 24 May. Cyclonic vortex signatures are indicated by solid black, blue, and red circles in (a), black in (b), and dotted black circle in (c); anticyclonic vortex signatures/TVSs are indicated by solid white circles in all panels. (a) 0205:30, (b) 0208:20, (c) 0211:10, and (d) 0214:16 UTC 24 May 2008. The height of the anticyclonic TVS is at (a) 430, (b) 390, (c) 340, and (d) 300 m AGL. The maximum ΔV in m s^{-1} is indicated next to each vortex signature/TVS. North is in the 360° direction. Range rings are shown every 2.5 km.

(i.e., the surface location of the anticyclonic tornado is displaced southward and eastward from the vortex aloft). The tilt may have resulted from the lower portion of the tornado having been advected southward and eastward by the RFGF (e.g., French et al. 2014, their Fig. 21) or from its track relative to a parent meso-anticyclone. The damage path appears to have been the widest when the tornado passed over the airport (Fig. 3b); this finding might be misleading because the airport presented the greatest concentration of structures that could be damaged. One must, therefore, be careful in correlating damage path width with tornado intensity when there is an irregular distribution of structures or natural objects in the path of a tornado.

While it was not possible to resolve the anticyclonic tornado using the TDWR data owing to insufficient spatial resolution (the range to the tornado was ~55 km,

so the 0.5°-wide beam was ~450–500 m across), the vortex parent to the anticyclonic tornado is seen as a region of anticyclonic shear at low levels (Fig. 4). An arc marking the leading edge of the RFGF is located along the zero isodop. From Fig. 4 we find that the couplets in Doppler shear were separated by ~5 km, while the approximate separation between the two damage paths was ~5 km; thus, the separation between the damage paths coincides roughly with separation between the vortex shear signatures, so we have confidence that the damage paths approximately coincide with the tracks of the parent vortex signatures. The southern portion of the leading edge of the RFGF is oriented approximately in the east–west direction, which is evidence that the tilt of the anticyclonic tornado noted in the previous paragraph was caused by a southward-surging portion of the RFGF.
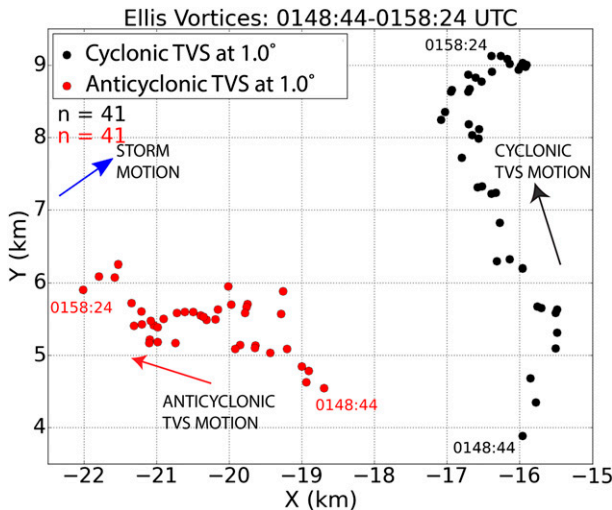
FIG. 8. The locations of the anticyclonic TVS (red dots) and cyclonic TVS (black dots) at 1° elevation angle in the first Ellis, KS, supercell, from MWR-05XP data on 23 May 2008; beginning and end times plotted in UTC on 24 May; data plotted every ~15 s. The abscissa and ordinate are plotted in km east of and north of, respectively, the location of the MWR-05XP. The blue arrow represents the approximate storm motion during a 20-min period centered on the analysis time based on data from the KDDC WSR-88D. The heights of the TVSs are at ~300 m ARL. The red and black arrows indicate the approximate motion of the anticyclonic and cyclonic TVSs, respectively.

The shear associated with the cyclonic vortex signature decreased between 0024:32 and 0027:37 UTC 25 April 2006 (Figs. 4a,b), consistent with the visual decay of the cyclonic tornado. The anticyclonic vortex shear signature associated with the anticyclonic tornado was weaker than its cyclonic counterpart. The anticyclonic vortex signature was located just to the west of the arc marking the RFGF, implying that the tornado was slightly behind the gust front.[3] The magnitude of the quasi-horizontal, azimuthal wind shear signature associated with the anticyclonic tornado as a function of time and height was estimated from the TDWR data (Fig. 5) in the same manner as was done by French et al. (2013) using MWR-05XP data. During the volume scan collected between 0024 and 0026 UTC, around 5 min prior to the appearance of damage (0030 UTC), the strongest anticyclonic shear signature (ΔV from the maximum outbound to maximum inbound) was located at a height less than 1 km AGL. Confidence in the assessment of the vertical trends in ΔV is reduced by the irregular scanning strategy used by the TDWR on this day, which resulted

---

[3] It is possible that the tornado was associated with an internal momentum surge as shown in another case (18 March 2012) later, but the spatial resolution of the KOKC TDWR radar was not sufficient at the relatively long range to resolve it well.
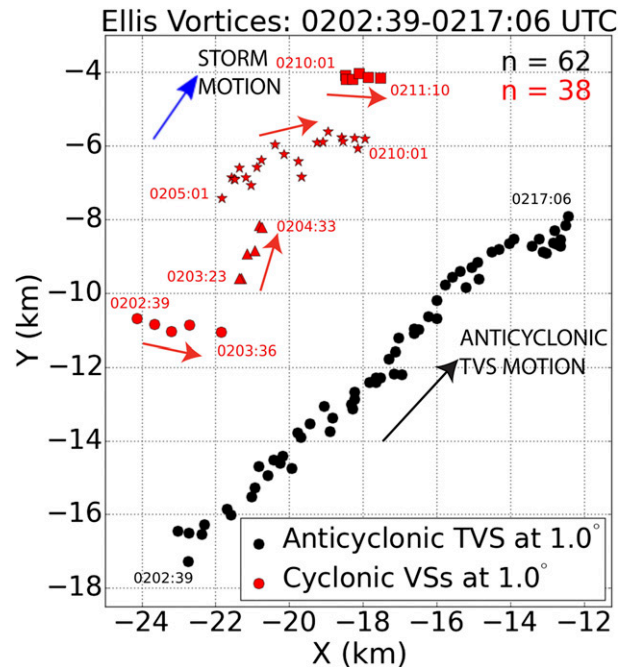

FIG. 9. As in Fig. 8, but for the later Ellis, KS, supercell, and for both the cyclonic and anticyclonic TVSs; the red and black arrows indicate the approximate motion of the cyclonic VSs and anticyclonic TVS, respectively. The individual cyclonic VSs are marked by different symbols and their locations were only plotted if they could be tracked for longer than 1 min in MWR-05XP data. The blue arrow represents the approximate storm motion during a 20-min period centered on the analysis time based on data from the KDDC WSR-88D. The heights of the TVSs and VSs are at 250–500 m ARL.

in poor temporal resolution for elevation angles that would have sampled the vortex above ~3 km AGL. No strong shear signature was evident at any altitude while damage was being inflicted (damage began at ~0030 UTC) because, unfortunately, data were not collected then and also when it dissipated (~0031–0036 UTC). The ΔV at ~2.5 km AGL increased from ~0025 to 0030/ 0031 UTC and decreased from the surface to 1 km AGL between 0028 and 0036 UTC. The shear signature ΔV was $>20\,\mathrm{m\,s^{-1}}$ above 4 km AGL only at the time we have data at these levels (i.e., ~0028–0031 UTC).

From the photographs of the tornado (Figs. 1 and 2) it can be seen that the region around it was mainly optically transparent, which is consistent with either no precipitation or only widely spaced precipitation particles and relatively weak radar reflectivity (not shown). This observation is significant because in the case of the former, anticyclonic tornadoes are not easily detected by radar because the backscattered signal is weak; in the case of the latter, the tornadoes may be easily detected, but without visible motions of rain curtains, the imminent formation of a tornado may not be recognized by spotters.
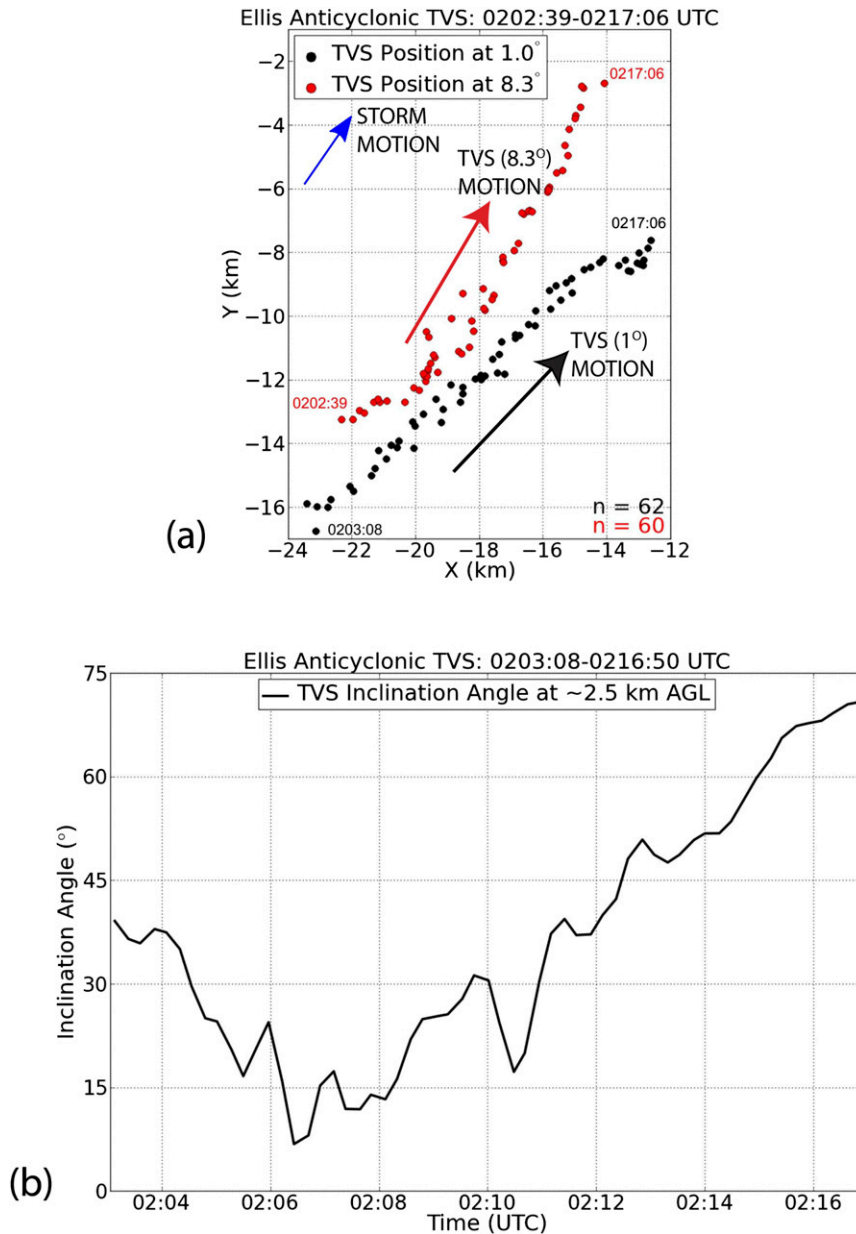
FIG. 10. Tilt of anticyclonic TVS for the later, Ellis, KS, anticyclonic TVS. (a) The locations of the anticyclonic TVS (black dots) at 1° elevation angle and at 8.3° elevation angle, from MWR-05XP data on 23 May 2008; beginning and end times are plotted in UTC on 24 May. The abscissa and ordinate are plotted in km relative to the location of the MWR-05XP; (b) TVS inclination angle vs time (UTC) on 24 May 2008 at ~2.5 km AGL. In (a), the blue arrow represents the approximate storm motion during a 20-min period centered on the analysis time based on data from the KDDC WSR-88D and the heights of the TVSs at 1.0° and 8.3° elevation angle are 250–500 m and 2.1–3.7 km ARL, respectively. The red and black arrows represent the approximate motion of the anticyclonic TVSs at 8.3° and 1°, respectively.

b. 23 May 2008

Two independent couplets of anticyclonic–cyclonic vorticity at low levels were documented in supercells by the MWR-05XP on 23 May 2008 near the town of Ellis in northwestern Kansas at ranges of 15–20 km and 15–25 km, respectively (Figs. 6 and 7). The first was associated with a TVS in just the cyclonic member, and damage was reported only from the cyclonic member (http://www.spc.noaa.gov/climo/reports/080523_rpts.html);
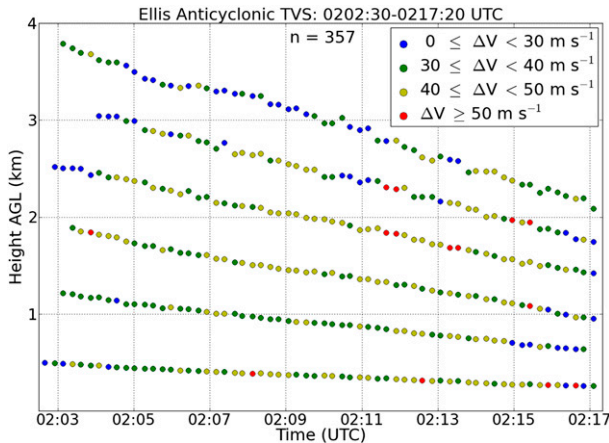
FIG. 11. Height of anticyclonic vortex signatures (TVSs) as a function of time in the second Ellis, KS, supercell on 23 May 2008, based on MWR-05XP data; times are plotted in UTC on 24 May 2008. Color code shown for ΔV (m s^{-1}) in insert at the upper right. The total number of measurements plotted (n) is 357.

the anticyclonic member was too weak to be considered a TVS. The second pair had TVSs, and tornadoes associated with both cyclonic and anticyclonic vortices (based on the closeness in time and space to reported tornadoes/damage to the TVSs). None of the tornadoes from either vortex pair were visible at the site of the radar because they were too far away, it was dark, and there was intervening precipitation.

The anticyclonic vortex of the first couplet at low levels propagated independently of the larger and more intense cyclonic vortex to its west or southwest (Figs. 6 and 8). The cyclonic TVS propagated to the west-northwest, to the left of the motion of the storm, consistent with the cyclic tornadogenesis process (Adlerman et al. 1999), while the subtornadic-intensity anticyclonic vortex, which was not associated with an observed tornado or damage, propagated more rapidly to the northnorthwest, then turned toward the northeast before it dissipated (Fig. 8).

Later, a broad area of cyclonic rotation, which earlier had contained numerous transient cyclonic VSs (Fig. 7a), was accompanied by a companion anticyclonic TVS to its south-southeast. There was a tornado reported in the area of the cyclonic VSs, but it is not known which of the cyclonic VSs was associated with the reported tornado. The anticyclonic TVS propagated to the northeast (Figs. 9 and 10a) in a direction similar to that of the storm, while the cyclonic VSs propagated generally eastward (Fig. 9), often well to the right (at least 45°) of estimated storm motion. The propagation characteristics of the anticyclonic–cyclonic couplets of the first set of tornadoes (Fig. 8) differed from those of the second (Fig. 9), perhaps a consequence of the anticyclonic

member of the couplet of the second being much stronger than the first or because cyclic tornadogenesis was no longer occurring. The anticyclonic TVS tilted to the northeast with height early and then to the northwest with height later (Fig. 10a) similar to high-resolution observations of northward tilt in cyclonic tornadoes (Wurman and Gill 2000; Alexander and Wurman 2005; Tanamachi et al. 2012; French et al. 2014). The TVS inclination angle was greatest during tornadogenesis and in the minutes leading up to and during dissipation (Fig. 10b), as was that of the cyclonic tornado in the Goshen County tornado during VORTEX2 (French et al. 2014). We speculate that the tilt increased with time during dissipation because low-level outflow advected the tornado away from the location of the vortex aloft (e.g., French et al. 2014).

It is not known exactly when the anticyclonic tornado associated with the anticyclonic TVS first formed, owing to contamination from second-trip echoes at some levels in MWR-05XP data. Two reports, at 0217 and 0218 UTC, were made to the local NWS of simultaneous tornadoes in the approximate area where MWR-05XP data show cyclonic VSs and an anticyclonic TVS at 1° elevation angle, the lowest observation level. However, both features had $\Delta V > 30$ m s^{-1} several minutes earlier, at ~0205 UTC (Fig. 7a). From 0203 to 0215 UTC, the intensity of the TVS associated with the anticyclonic tornado was tracked in time and height (Fig. 11). Anticyclonic shear was relatively steady ($35 < \Delta V < 45$ m s^{-1}) at heights of 500 m to 2.5 km above radar level (ARL); TVS intensity was generally weaker up to 3.5 km ARL, above which no temporally consistent TVS could be tracked (Fig. 11). Beginning at 0215 UTC, TVS intensity began to decrease in the lowest 1 km ARL. Subsequently, at 0217:20 UTC, there was a 90-s data gap, after which the TVS could no longer be tracked.

c. 18 March 2012

A supercell in southwestern Oklahoma produced several tornadoes on 18 March 2012 near Mangum and Willow (http://www.spc.noaa.gov/climo/reports/120318_rpts. html). The cumulonimbus cloud, as seen to the west several minutes prior to the tornado, was bell shaped (e.g., Bluestein and Parks 1983) with a laminar, striated base (Fig. 12a). Two regions of opaque precipitation were visible: one underneath the middle of the cloud base (left arrow) and one (not as opaque) to the north of most of the cloud base (right arrow). A few minutes later, scud clouds appeared under the cloud base, to the left of the southernmost, opaque precipitation area, just to the right of the utility pole (Fig. 12b). The appearance of scud has been associated with evaporatively cooled air that is being lifted and the formation of a wall cloud
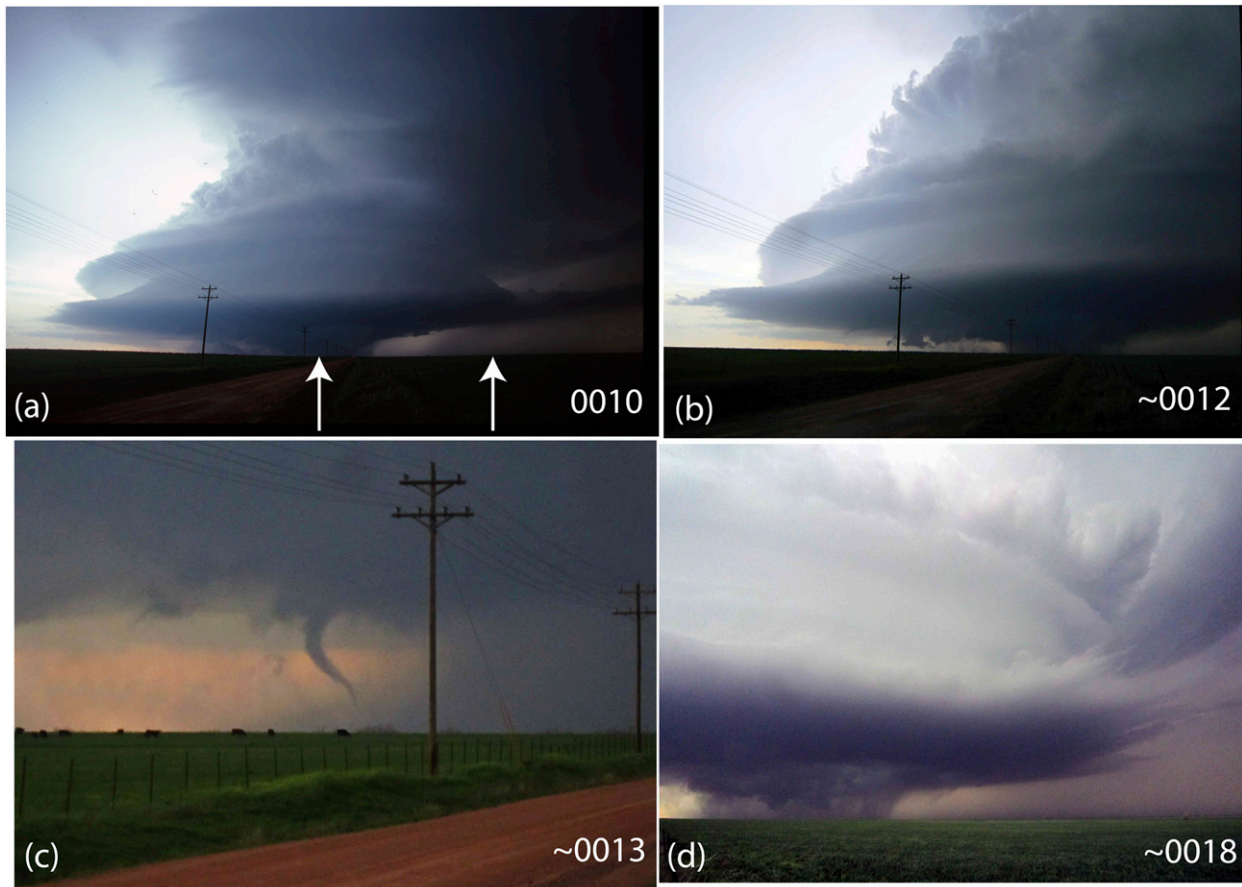
FIG. 12. Photographs of the Willow, OK, supercell on 18 Mar 2012. (a) Wide-angle view to the west-southwest at 0010 UTC 19 Mar; left and right arrows point to southern and northern areas of opaque precipitation regions, respectively; (b) view to the west/west-southwest of the southern portion of the supercell at ~0012 UTC, showing the southern opaque precipitation region and scud to its south (left, near the utility pole); (c) zoomed-in view of the anticyclonic tornado to the west-southwest at ~0013 UTC; and (d) view to the northwest of the northern part of the supercell, showing the clear slot, lowered cloud bases, and the northern precipitation region at ~0018 UTC. (Photographs courtesy of H. Bluestein.)

(Bluestein and Parks 1983; Rotunno and Klemp 1985; Atkins et al. 2014). Atkins et al. (2012) found a wall cloud in a region of low-level anticyclonic vorticity in another tornadic supercell (their Fig. 4), but no anticyclonic tornado was observed. While the mobile radar crew was focused on the area just to the left of the northernmost precipitation region, to the right of the main cloud base, an anticyclonic tornado suddenly appeared to the west-southwest, near the southern edge of the opaque region of precipitation on the southern end of the cumulonimbus (Fig. 12c), to the left of the middle utility pole seen in Figs. 12a and 12b. This tornado lasted only ~1 min or less, after which lowered cloud fragments and a clear slot (Lemon and Doswell 1979) appeared under the right side of the cloud base. A cyclonic tornado (not shown) appeared under the right side of the cloud base (Fig. 12d), ~5 km west-northwest of Willow, approximately 14 min later.

The closest (i.e., east and northeast) edge of the main cloud base was associated with the leading edge of a RFGF (labeled "1" in Fig. 13). From the radar imagery acquired at the time the anticyclonic tornado was observed, a hook echo and low-level mesocyclone are seen to the northwest of the radar while a feature having some characteristics of an internal rear-flank downdraft momentum surge (labeled "2" in Fig. 13) (e.g., Wurman et al. 2007; Marquis et al. 2008; Lee et al. 2012; Kosiba et al. 2013; Skinner et al. 2014) was evident to the rear of the edge of the RFGF. At the southern end of the internal rear-flank downdraft momentum surge there was a small area of anticyclonic shear in the Doppler velocity; the brief anticyclonic tornado (Fig. 12c) formed in this area. Kosiba et al. (2013) documented an anticyclonic vortex along an internal momentum surge in another tornadic supercell. The southernmost opaque are of precipitation seen in Fig. 12a was located near the
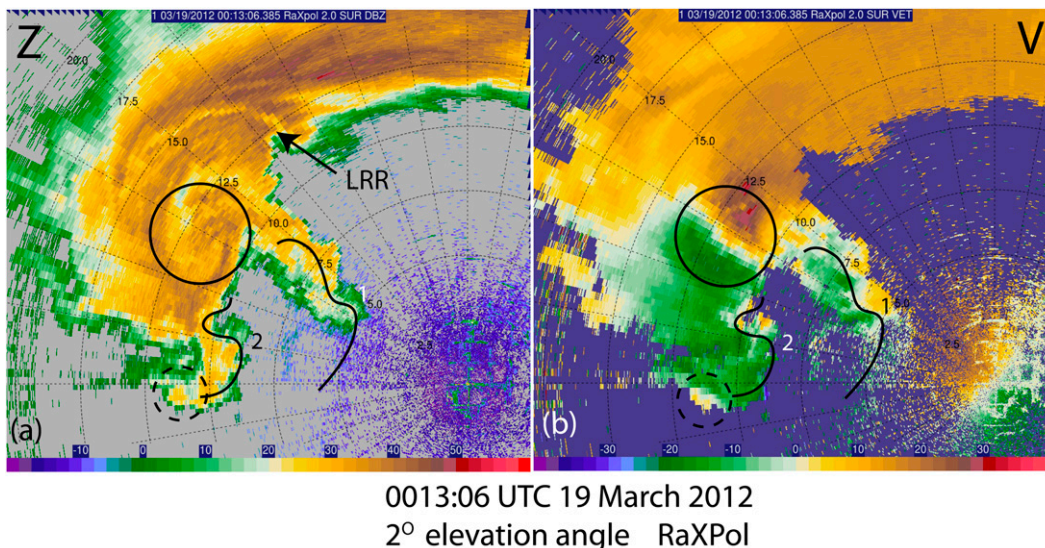
FIG. 13. RaXPol imagery of the Willow, OK, supercell on 18 Mar 2012. (a) Radar reflectivity factor Z (color coded in dBZ) and (b) Doppler velocity V (color coded in m s^{-1}) at 2° elevation angle, at 0013:06 UTC 13 Mar 2012, the approximate time of the anticyclonic tornado. The solid circle in (a) is at the tip of the hook echo and in (b) it also marks the location of the cyclonic-shear vortex signature; the dashed circle in both panels marks the location of the anticyclonic vortex signature. The solid lines labeled as "1" and "2" mark the leading rear-flank gust front and a secondary, internal momentum surge, respectively. The spacing of the range markings is 2.5 km; range rings are labeled in km in (b). It is hypothesized that the anticyclonic tornado, which was to the west-southwest of the east–west road seen in Fig. 12c, was probably located near the anticyclonic vortex signature. North is in the 360° direction.

southeasternmost part of the hook echo (Fig. 13a); the northernmost area of precipitation was located to the north of the hook echo. A low-reflectivity ribbon (LRR) (Wurman et al. 2012; Snyder et al. 2013; Griffin et al. 2015) is seen in this area also, though the significance of it is not known. The LRR is noted, however, in the event, after documentation of many more cases, it turns out to be a feature that may be correlated with the occurrence of tornadoes. Unlike the anticyclonic tornadoes observed on 24 April 2006 and 23 May 2008, the anticyclonic tornado on 18 March 2012 was very short lived and no TVS could be identified in the data, either because it occurred in between radar scans or because the backscattered signal was too weak.

d. 31 May 2013

A supercell near El Reno, Oklahoma, on 31 May 2013 produced a number of tornadoes (Wurman et al. 2014; Bluestein et al. 2015) (Fig. 8 in Bluestein et al. 2015; Fig. 14 here). One of these was anticyclonic (Fig. 15, labeled as "T3" in Fig. 14) and formed to the southeast of the large, cyclonic tornado (labeled as "T2" in Fig. 14). The track of the main cyclonic tornado was to the left of the track of the anticyclonic tornado, especially when the latter turned to the right during the second half of its life (Fig. 14b). There was also an area of strong anticyclonic shear before and to the west of the

longer-lived, EF2 anticyclonic tornado, but it was short lived (not shown).

During the time that the anticyclonic tornado was occurring, RaXPol was scanning through a relatively shallow volume to maximize spatiotemporal resolution in the lower part of the storm.[4] As such, to get a better understanding of the vertical evolution of the vortex through a deeper layer, data from the Oklahoma City TDWR were examined. The anticyclonic TVS observed by the TDWR began at low altitude and built upward with time intermittently (Fig. 16); it was most intense, at low altitude, from ~2335 to 2338 UTC. It decayed abruptly after 2338 UTC, even though it was reported as late as 2341 UTC (Fig. 14). The anticyclonic tornado formed to the southeast of the larger, cyclonic tornado

---

[4] Although the radar had been leveled by 2335 UTC, at 2332:10 UTC, the time at which RaXPol data are plotted in Figs. 17 and 18, the radar truck, based on pitch and roll sensor data, was pointed down ~3.3° in the direction of the tornado. For an antenna elevation angle of 3°, the antenna was pointed ~0° relative to the true horizontal for those azimuths near the tornado. For this orientation, some of the beam may have hit the ground, producing some contamination of Doppler velocity measurements. A decrease in elevation with range in the direction of the tornado, however, probably mitigated contamination. There likely were other appreciable complexities in the illuminated radar beam pattern owing to interaction with the ground as discussed in Snyder et al. (2015).
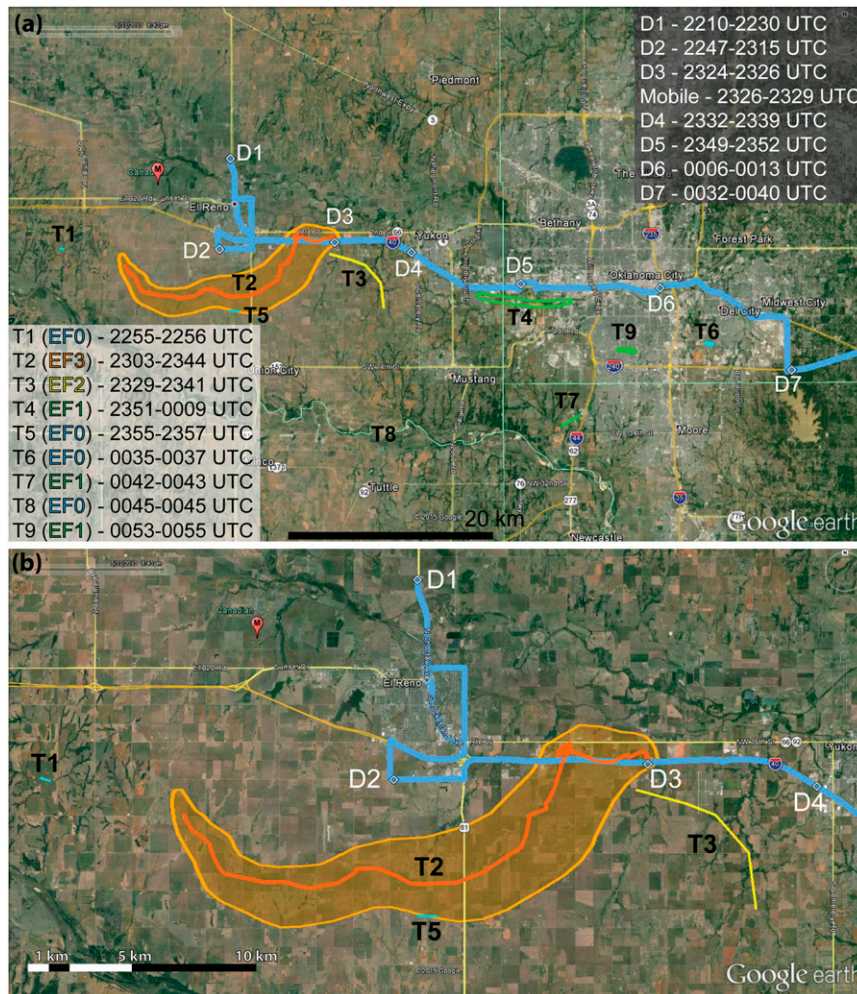
FIG. 14. Locations of the deployments of RaXPol (a) for a broad view and (b) for a zoomed-in view, with respect to tornadoes (T1–T9) and other geographic features on 31 May 2013. All deployment locations (D1–D7) and tornado tracks (color coded, along with NWS EF ratings on inset) are shown in (a) along with the track of RaXPol (blue). Only deployment spots D1 (2210–2230), D2 (2247–2315), D3 (2324–2326), mobile (2326–2329), and D4 (2332–2339) (all times in UTC) are shown in (b). The red pushpin marked with "M" is the location of the El Reno mesonet site. The large tornado damage path is outlined in orange, with the path taken by the center of the Doppler radar vortex signature given in orange; the anticyclonic tornado path is given in yellow. Damage tracks and EF ratings are courtesy of the NWS. From Bluestein et al. (2015). For this study, the most relevant markings in (b) are the location of the large, cyclonic tornado T2, the anticyclonic tornado T3, and the deployment site D4.

to its west-northwest (Fig. 17) and was also associated with a tornadic debris signature (TDS) identifiable by low ρ_{hv} and low Z_{DR} [as also noted by Wurman et al. (2014) in KTLX and DOW data; they also noted multiple vortices in DOW data].

The vertical structure of the anticyclonic tornado as observed by RaXPol provides what may be the highest-resolution examination to date of an anticyclonic tornado in a supercell, but only below ~650 m ARL. Just before the anticyclonic tornado was most intense (at

least as measured by ΔV), but when the "debris ball" was most evident in the reflectivity field nearest the ground, there was no weak-echo column (WEC) (Fig. 18a); the WEC is thought to be the result of the centrifuging radially outward of the scatterers, mostly of the most massive scatterers (e.g., Wakimoto and Martner 1992; Bluestein et al. 2007a; Dowell et al. 2005; Tanamachi et al. 2012), although the internal structure of the flow within the tornado may yield trajectories that move outward with height. Vertical columns of low Z_{DR}
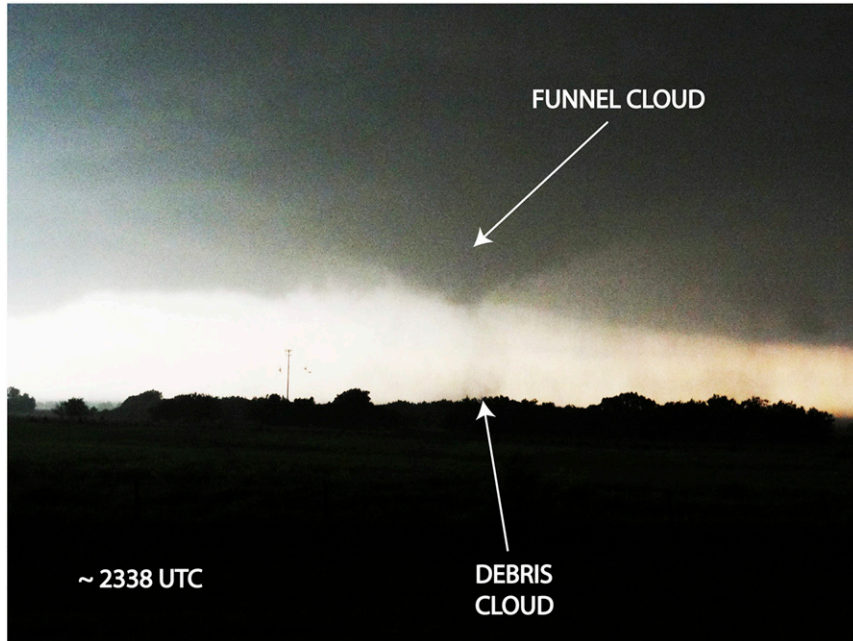
FIG. 15. Photograph of the end of the anticyclonic tornado (T3 in Fig. 13) from deployment site (D4 in Fig. 13), at ~2338 UTC 31 May 2013, as viewed to the southwest. (Photograph courtesy of H. Bluestein.)

(Fig. 18b) and low ρ_{hv} (Fig. 18c) were coincident with the anticyclonic vortex signature (Fig. 18d). Such low values of Z_{DR} and ρ_{hv} have been associated with debris (e.g., Ryzhkov et al. 2005; Bluestein et al. 2007b). The strongest Doppler velocities were $\sim -50 \, \text{m s}^{-1}$ $\sim 300 \, \text{m}$ AGL and above. The Doppler-velocity pattern is asymmetric about zero velocity because the tornado had a component of motion toward the radar. Since it is unusual that there was no WEC, it is possible that the size of the debris particles was small (e.g., dust particles) and, therefore, some debris may not have been centrifuged radially outward enough to cause a reduction in the radar reflectivity near the axis of rotation, or that the radar beam was too low.

4. Summary and discussion

Four cases of the genesis of anticyclonic tornadoes in supercells in which a cyclonic tornado was also observed are discussed. In three of these cases (24 April 2006, 23 May 2008, and 31 May 2013), a companion cyclonic tornado either had recently dissipated or was still present, but weakening. In one case (18 March 2012), the anticyclonic tornado formed before any cyclonic tornado formed. In general, these cases are similar to those described by Brown and Knupp (1980), Fujita (1981), Bluestein et al. (2007b), and Wurman and Kosiba (2013), in that there were companion cyclonic and

anticyclonic vortices at either end of a rear-flank gust front/bulging hook echo. The Iowa case (13 June 1976), however, had the strongest anticyclonic tornado. These cases, however, are different from those in which short-track "satellite" anticyclonic tornadoes in supercells producing cyclonic tornadoes have been documented (e.g., Tanamachi et al. 2012).

Since there is no systematic relationship between the formation and dissipation of cyclonic and anticyclonic
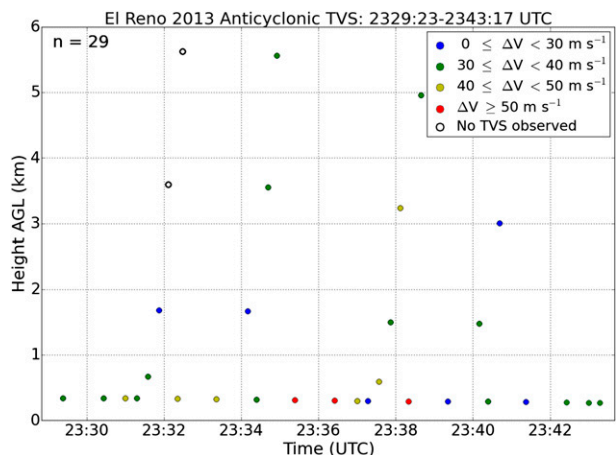

FIG. 16. As in Fig. 5, but for the El Reno, OK, anticyclonic tornado on 31 May 2013; for $n = 29$ measurements. Data are not plotted above 6 km AGL (8–20 km AGL), where no TVS was ever observed.
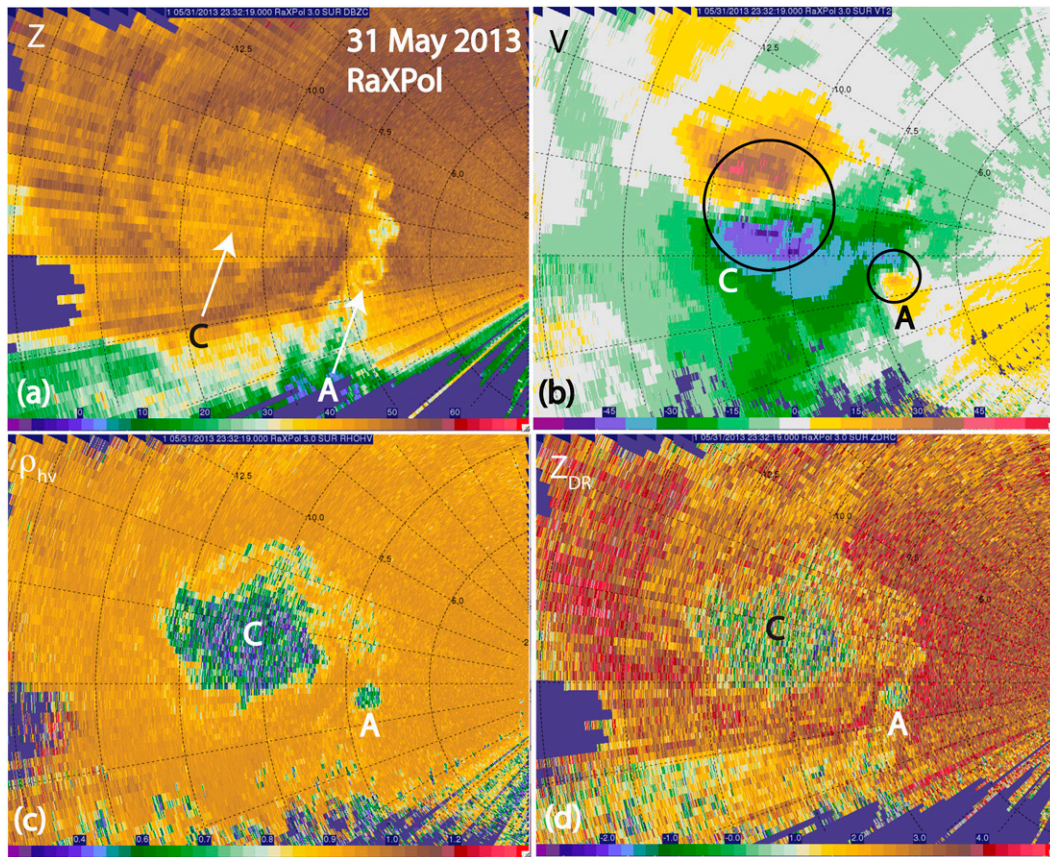
FIG. 17. Storm-scale view of the El Reno, OK, tornadic supercell of 31 May 2013, from RaXPol, at 2332:19 UTC. (a) Radar reflectivity factor Z in dBZ, (b) Doppler velocity V in m s^{-1}, (c) copolar cross-correlation coefficient ρ_{hv}, and (d) differential reflectivity Z_{DR} in dB. Locations of cyclonic (C) and anticyclonic (A) vortex signatures associated with the tornadoes are indicated. Range markers shown every 2.5 km. The radar was not level at this time; the elevation of the beam angle in the direction of the tornadoes, however, was ~0°, and as much as 3° in the opposite direction. North points to the top of each panel.

tornadoes in this very small sample size, there does not appear to be an obvious causal relationship between the generation or dissipation of the cyclonic tornado and the generation of the anticyclonic tornado. However, in all cases of the appearance of an anticyclonic tornado there was at least a companion low-level mesocyclone at the time of the genesis of the anticyclonic tornado.

In all cases documented herein, the main cyclonic tornado was located in its "typical" location for mesocyclone-associated tornadoes in cyclonically rotating supercells—at the tip of a bulging RFGF near a low-level mesocyclone (Figs. 4, 7, 13, and 17). The anticyclonic tornado was located at the trailing end of the RFGF (Figs. 4, 7, and 17) or, in the case on 18 March 2012, at the trailing end of an internal rear-flank momentum surge (and possibly also in the case on 24 April 2006) (Fig. 13). It is believed that the 18 March 2012 case is the first one in which the anticyclonic tornado (of an anticyclonic–cyclonic pair) was located at the end of an

internal surge rather than along the leading RFGF surge. Since the sample size of all anticyclonic–cyclonic tornado pairs is small, we cannot conclude whether or not this occurrence is rare or common. Kosiba et al. (2013) documented anticyclonic vortices down to ~200 m AGL along an internal surge, but the vortices were, however, not tornadic. It is not known why in the case discussed by Kosiba et al. (2013) the vortices failed to produce tornadoes, while in the 18 March 2012 case a tornado was in fact produced. We speculate that perhaps the surface air in the latter case was not as cold and negatively buoyant as the surface air in the former, but have no temperature data for the latter to test our hypothesis.

From Figs. 3, 8, 9, and 14 we find that the tracks of the cyclonic and anticyclonic tornadoes or vortex signatures diverged; this was also the case described by Bluestein et al. (2007b, their Fig. 10). Brown and Knupp (1980), however, found in their case that the tracks were parallel. In other cases track data were not available [e.g.,
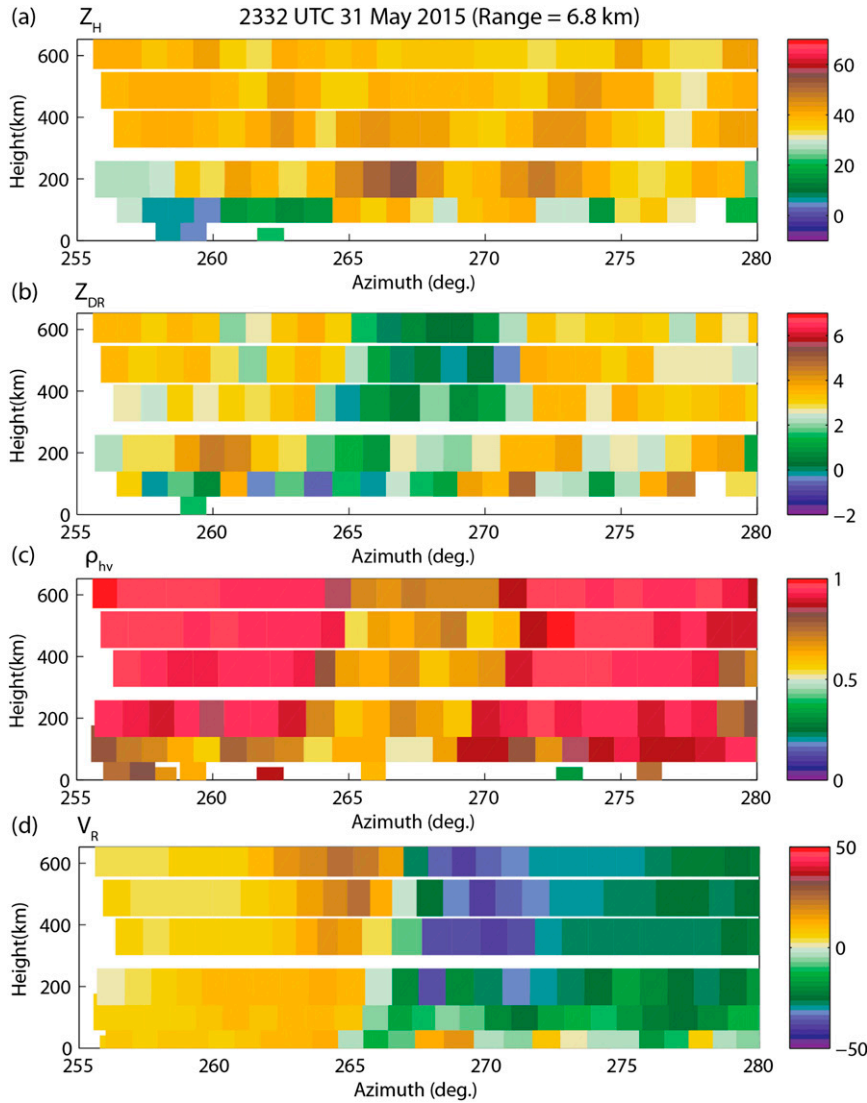
FIG. 18. Vertical cross section through the anticyclonic tornado in the El Reno, OK, supercell of 31 May 2013 at 2332 UTC, from RaXPol. Azimuth (abscissa) vs height (m AGL) at a range of 6.8 km. (a) Radar reflectivity factor of the horizontally polarized beam (Z_H) in dBZ, (b) differential reflectivity Z_{DR} in dB, (c) copolar cross-correlation coefficient ρ_{hv}, and (d) Doppler velocity V_R in m s^{-1}. Color codes are at the right-hand side of each panel. The distance of 5° in azimuth at 6.8-km range is ~600 m.

Fujita (1981), 4 June 2015; Table 1]. It is possible that the divergence in the tracks could be a result of the cyclonic tornadoes either being advected by the cyclonic background flow (associated with the low-level mesocyclone) or continuing on without changing direction, while the anticyclonic tornadoes turn to the right as the gust front spreads out and the background wind to the rear of the trailing part of the RFGF veers to more northerly from northwesterly or westerly at the southern end. When the tracks of the cyclonic and anticyclonic tornadoes diverge, the NWS may mislead

the public if a tornado warning includes only the motion of the larger, companion cyclonic tornado. During the anticyclonic tornado of 24 April 2006 the tornado-warned area for the cyclonic tornado did not include the area actually hit by the anticyclonic tornado to the south.

Anticyclonic–cyclonic couplets of vorticity along the RFGF as seen in Figs. 4, 7, 13, and 17 are commonly observed in supercells, as has been documented in many observational and modeling studies, including Bluestein and Gaddy (2001), Straka et al. (2007), Markowski et al.
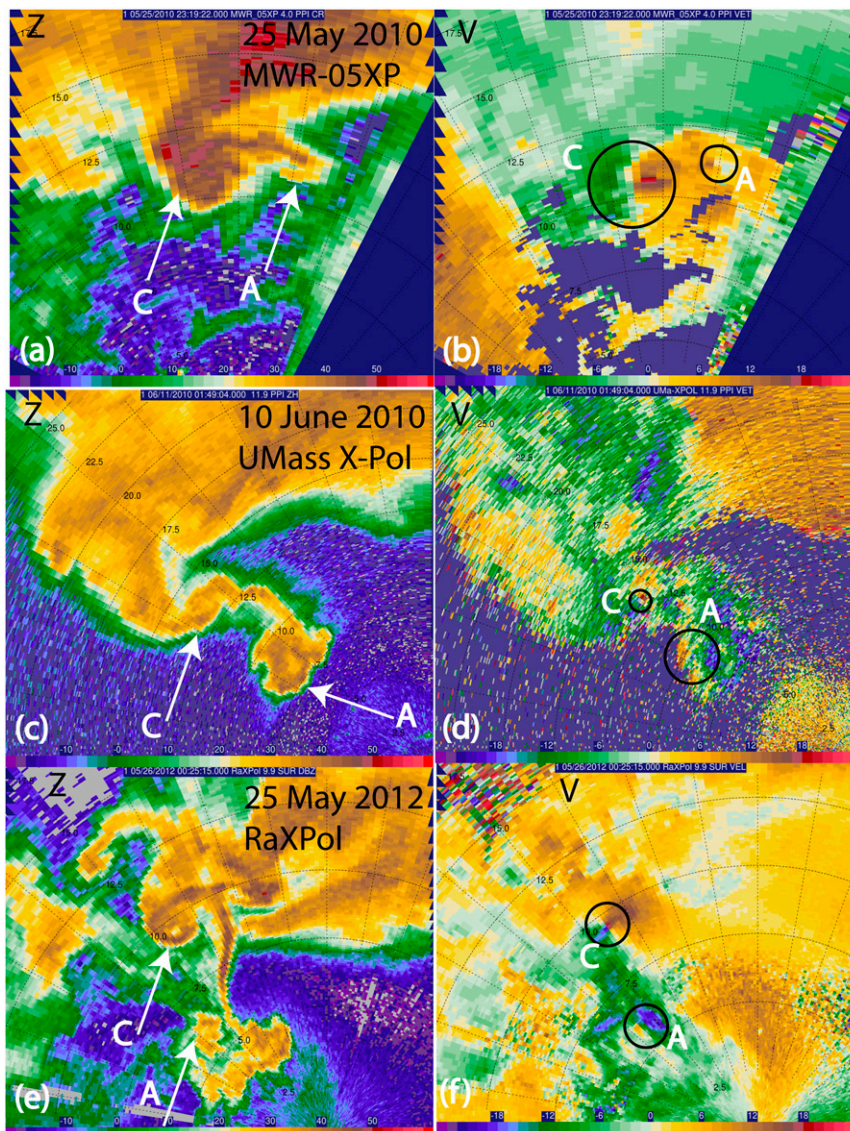
FIG. 19. Examples of cyclonic–anticyclonic vorticity couplets in supercells from three different mobile, X-band, Doppler radars. (a) Radar reflectivity Z in dBZ and (b) Doppler velocity in m s^{-1} for the MWR-05XP, at 2319:22 UTC 25 May 2010 at 4° elevation angle, in western Kansas–eastern Colorado [this case is described in Bluestein et al. (2014)]; (c),(d) as in (a),(b), but for the University of Massachusetts X-band Polarimetric (UMass X-Pol) radar [UMass X-Pol described in Tanamachi et al. (2012)], at 0149:04 UTC 11 Jun 2010 at 11.9°, eastern Colorado; and (e),(f), as in (a),(b), but for RaXPol, at 0025:15 UTC 26 May 2012 at 9.9°, western Kansas. Range rings are plotted every 2.5 km. In (a),(c), and (e), the cyclonic (C) and anticyclonic (A) hook echoes are highlighted by arrows. The corresponding Doppler shear signatures are highlighted by circles in (b),(d), and (f). North is in the 360° direction.

(2008), Bluestein et al. (2010), Wakimoto et al. (2012), Markowski and Richardson (2014), Wurman and Kosiba (2013), and others; they have also been documented along internal momentum surges (Kosiba et al. 2013). Figure 19 shows a sample of other anticyclonic–cyclonic couplets documented by the authors using various mobile Doppler radars [e.g., other than by the Doppler on Wheels, as in

Wurman and Kosiba (2013)]. In contrast with the other cases examined in this paper, no anticyclonic tornadoes were observed in any of the examples shown in Fig. 19.

In the cases we have examined, no evidence was found of any series of anticyclonic vortices along the gust front or internal surge, like those series of vortices simulated in nonsupercell convective storms by Lee and

TABLE 3. Estimated environmental parameters for the storms in Table 1.

UTC time and date model source	CAPE (J kg^{-1}) (most unstable)	0–6-km vector difference (m s^{-1})	SRH (m^2 s^{-2})	Damage
NOAA–CIRES twentieth-century reanalysis (V2c)				
1800 UTC 13 Jun 1976	2567	15	24	F3
NARR				
0000 UTC 4 Jun 1980	3907	19	240	F3, F1
NAM				
0000 UTC 30 May 2004	4499	25	386	F1
RUC				
0000 UTC 25 Apr 2006	3211	21	77	F1
0300 UTC 24 May 2008	2466	34	1075	EF0
0200 UTC 30 May 2008	2373	26	832	EF0
0000 UTC 19 Mar 2012	1785	18	330	—
RAP				
0000 UTC 1 Jun 2013	3029	27	415	EF3
0000 UTC 5 Jun 2015	2477	18	111	EF0

Wilhelmson (1997). The visual appearance of the 24 April 2006 anticyclonic tornado (e.g., Fig. 2), however, was very similar to observed landspouts [cf. Fig. 5 in Beebe (1955); e.g., little change in the visual width of the tornado with height, narrow and short funnel below cloud base, a slender and translucent cylinder/tube of debris between the ground and cloud base, etc.]. The similar visual appearance may be some evidence that the primary mechanism(s) driving the 24 April 2006 anticyclonic tornado may have been similar to those associated with some landspouts or so-called "nonsupercell tornadoes."

To see if there are special environmental conditions supportive of anticyclonic tornadoes in cyclonically rotating, right-moving supercells, environmental soundings and hodographs were estimated from model data (Table 3). It was not anticipated that the soundings and hodographs would differ from those typically found in cyclonically rotating supercells, but we wanted to find out if any characteristics tended to be extreme or cluster about some limited range. Markowski and Richardson (2014) suggested, for example, that relatively high low-level vertical shear may be necessary (along with a relatively weak surface cold pool) for the production of relatively strong anticyclonic vortices. They found that the source of vorticity for the anticyclonic vortices was the baroclinic generation of horizontal vorticity along the leading edge of the cold pool; this vorticity is subsequently tilted near the main updraft so that the vortex line associated with the baroclinically generated vorticity is lifted and fractured and joined together with a vortex line associated with higher-level environmental horizontal vorticity that is tilted downward [Figs. 7 and 25d in Markowski and Richardson (2014)]. They attributed the sign and magnitude of the solenoidal generation to "details in the trajectories and their residence times in" the baroclinic zone.

It is seen that in nine known cases (four discussed here and five referenced elsewhere) where anticyclonic tornadoes were produced in cyclonically rotating supercells, the "most unstable" convective available potential energy (CAPE), that is, in the majority of these cases using the surface temperature and dewpoint temperature (assuming reversible moist adiabatic ascent and including latent heat of fusion), ranged from just under 2000 to almost 4500 J kg^{-1}. Thompson et al. (2003), in comparison, found that the mean mixed-layer CAPE, which is often no greater than the surface-based CAPE, ranged, in their sample of model-based proximity soundings, from ~2800 J kg^{-1} in supercells that spawned tornadoes that produced damage of F2–F5 intensity, down to ~1600 J kg^{-1} in supercells that did not produce tornadoes, and down to only ~1300 J kg^{-1} in nonsupercells. The magnitude of the vector difference of the wind over the lowest 6 km ranges, in the nine cases listed in Table 1, from 15 to almost 35 m s^{-1} and the storm-relative [storm motion was calculated using the pressure-weighted mean wind between 850 and 300 hPa modified using the method of Davies-Jones et al. (1990)] helicity ranges widely, from around 25 to over 1000 m^2 s^{-2}. Thompson et al. (2003), again in comparison, found that the mean 0–6-km shear was 25 m s^{-1} for the supercells that produce F2–F5 tornadoes and only ~8 m s^{-1} for the non-supercells; the 0–3-km storm-relative helicity ranged from 250 m^2 s^{-2} for the former and only ~50 m^2 s^{-2} for the latter. The estimated environmental hodographs (Fig. 20) all have clockwise turning of the wind vector with height at low levels. In all but one case (18 March 2012), the soundings were characterized by a low-level moisture layer capped by a stable layer and a drier, deep layer of more rapid decrease of temperature with height (not shown). In summary, the environmental conditions appear to be similar to those of right-moving, cyclonically rotating, supercells and no characteristic stands out
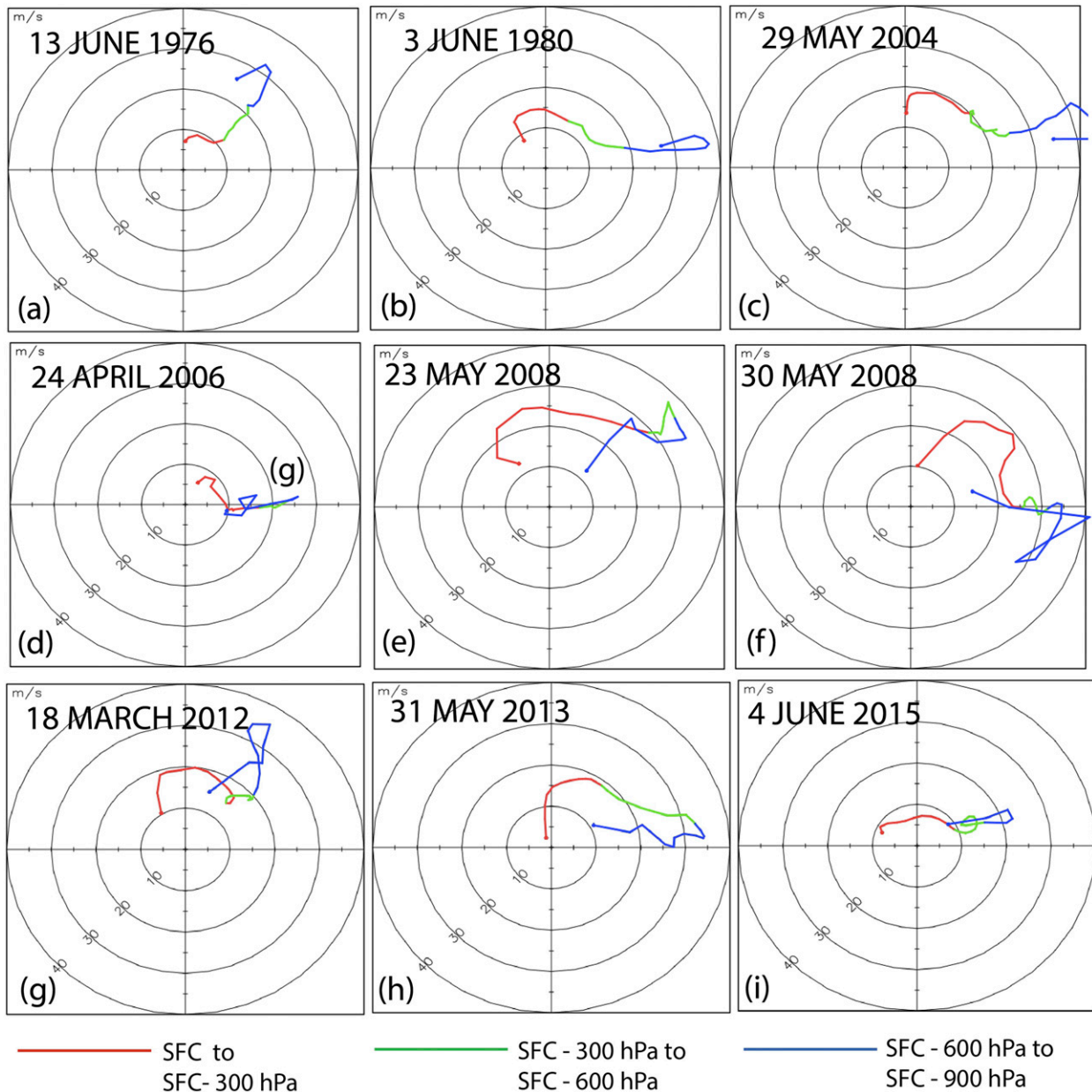
FIG. 20. Proximity hodographs for the cases listed in Table 1. The red segments extend from the surface to the surface less 300 hPa, the green extends from the surface less 300 hPa to the surface less 600 hPa, and the blue extends from the surface less 600 hPa to the surface less 900 hPa; thus, the red and green sections together show approximately the surface–5-km hodographs. (a) 1800 UTC 13 Jun 1976 over central Iowa; (b) 0000 UTC 4 Jun 1980, the 3 Jun 1980 Grand Island, NE, storm; (c) as in (a), but for 0000 UTC 30 May 2004, the 29 May 2004 storm near Calumet, OK; (d) as in (a), but for 0000 UTC 25 Apr 2006, the 24 Apr 2006 storm near El Reno, OK; (e) as in (a), for 0300 UTC 24 May 2008, the 23 May 2008 Ellis, KS, storms; (f) as in (a), but for 0000 UTC 30 May 2008, the 29 May 2008 Glen Elder, KS, storm; (g) as in (a), for 0000 UTC 19 Mar 2012, the 18 Mar 2012, the storm near Willow, OK; (h) as in (b), but for 0000 UTC 1 Jun 2013, the 31 May 2013 El Reno storm; and (i) as in (b), but for 0000 UTC 5 Jun 2015, the 4 Jun 2015 Simla, CO, storm.

as being unusual. While caution must be exercised in interpreting the parameters shown in Table 3 and the hodographs shown in Fig. 20, owing to the variations in the methods/models used to estimate them, it does appear that it is not possible to define, using the data available to us, a special environment for supercells that are both right moving/cyclonically rotating and that produce anticyclonic tornadoes. Overall, most of the cases (7/9) occurred in late May or the first half of June, when CAPE is climatologically high; only two cases

were identified earlier in the season. Based on the results of Markowski and Richardson (2014), the strength of a storm's cold pool, which we could not measure, could be an important factor. However, the physical mechanisms that control cold-pool intensity are complex, involving the details of the environmental hodograph, cloud microphysics, and the thermodynamic profile; given limited observations, these are often very difficult to ascertain.

The results of this study do not answer conclusively the question of how anticyclonic tornadoes form in right-moving, cyclonically rotating supercells, although, as with cyclonic tornadoes in cyclonic supercells, it seems quite likely that multiple mechanisms may be capable of producing them. In two of the cases (24 April 2006 and 31 May 2013) the vortex signature first appeared at low levels and propagated or was advected upward. Therefore, in these cases tornadogenesis occurred without a preexisting midlevel mesoanticyclone and may have been similar to landspout formation. In one of the cases (23 May 2008), the data were not of high enough quality (owing to second-trip contamination) to resolve tornadogenesis. In another one of the cases, the tornado was short lived and tornadogenesis was not resolved (12 March 2012), but there was circumstantial evidence that an internal RFD momentum surge may have played a role. We look forward to better documentation and to numerical experiments to elucidate further the formation of anticyclonic tornadoes in right-moving, cyclonically rotating supercells.

REFERENCES

Adlerman, E. J., K. K. Droegemeier, and R. Davies-Jones, 1999: A numerical simulation of cyclic mesocyclogenesis. *J. Atmos. Sci.*, **56**, 2045–2069, doi:10.1175/1520-0469(1999)056<2045:ANSOCM>2.0.CO;2.

Agee, E. M., J. T. Snow, and P. R. Clare, 1976: Multiple vortex features in the tornado cyclone and the occurrence of tornado families. *Mon. Wea. Rev.*, **104**, 552–563, doi:10.1175/1520-0493(1976)104<0552:MVFITT>2.0.CO;2.

Alexander, C. R., 2010: A mobile radar based climatology of supercell tornado structure and dynamics. Ph.D. dissertation, University of Oklahoma, Norman, OK, 229 pp.

——, and J. Wurman, 2005: The 30 May 1998 Spencer, South Dakota, storm. Part I: The structural evolution and environment of the tornadoes. *Mon. Wea. Rev.*, **133**, 72–97, doi:10.1175/MWR-2855.1.

Atkins, N. T., A. McGee, R. Ducharme, R. M. Wakimoto, and J. Wurman, 2012: The LaGrange tornado during VORTEX2. Part II: Photogrammetric analysis of the tornado combined with dual-Doppler radar data. *Mon. Wea. Rev.*, **140**, 2939–2958, doi:10.1175/MWR-D-11-00285.1.

——, E. M. Glidden, and T. M. Nicholson, 2014: Observations of wall cloud formation in supercell thunderstorms during VORTEX2. *Mon. Wea. Rev.*, **142**, 4823–4838, doi:10.1175/MWR-D-14-00125.1.

Beebe, R. G., 1955: A tornado development, 17 August 1953. *Bull. Amer. Meteor. Soc.*, **36**, 344–347.

Bluestein, H. B., 1985: The formation of a "landspout" in a "broken-line" squall line in Oklahoma. Preprints, *14th Conf. on Severe Local Storms*, Indianapolis, IN, Amer. Meteor. Soc., 267–270.

——, 2013: *Severe Convective Storms and Tornadoes: Observations and Dynamics*. Springer–Praxis, 456 pp.

——, and C. R. Parks, 1983: A synoptic and photographic climatology of low-precipitation severe thunderstorms in the Southern Plains. *Mon. Wea. Rev.*, **111**, 2034–2046, doi:10.1175/1520-0493(1983)111<2034:ASAPCO>2.0.CO;2.

——, and S. G. Gaddy, 2001: Airborne pseudo-dual-Doppler analysis of a rear-inflow jet and deep convergence zone within a supercell. *Mon. Wea. Rev.*, **129**, 2270–2289, doi:10.1175/1520-0493(2001)129<2270:APDDAO>2.0.CO;2.

——, C. C. Weiss, M. M. French, E. M. Holthaus, and R. L. Tanamachi, 2007a: The structure of tornadoes near Attica, Kansas, on 12 May 2004: High-resolution, mobile, Doppler radar observations. *Mon. Wea. Rev.*, **135**, 475–506, doi:10.1175/MWR3295.1.

——, M. M. French, R. L. Tanamachi, S. Frasier, K. Hardwick, F. Junyent, and A. L. Pazmany, 2007b: Close-range observations of tornadoes in supercells made with a dual-polarization, X-band, mobile Doppler radar. *Mon. Wea. Rev.*, **135**, 1522–1543, doi:10.1175/MWR3349.1.

——, ——, I. PopStefanija, R. T. Bluth, and J. B. Knorr, 2010: A mobile, phased-array Doppler radar for the study of severe convective storms: The MWR-05XP. *Bull. Amer. Meteor. Soc.*, **91**, 579–600, doi:10.1175/2009BAMS2914.1.

——, J. B. Houser, M. M. French, J. C. Snyder, G. D. Emmitt, I. PopStefanija, C. Baldi, and R. T. Bluth, 2014: Observations of the boundary layer near tornadoes and in supercells using a mobile, collocated, pulsed Doppler lidar and radar. *J. Atmos. Oceanic Technol.*, **31**, 302–325, doi:10.1175/JTECH-D-13-00112.1.

——, J. C. Snyder, and J. B. Houser, 2015: A multiscale overview of the El Reno, Oklahoma, tornadic supercell of 31 May 2013. *Wea. Forecasting*, **30**, 525–552, doi:10.1175/WAF-D-14-00152.1.

Bodine, D. J., M. R. Kumjian, R. D. Palmer, P. L. Heinselman, and A. V. Ryzhkov, 2013: Tornado damage estimation using polarimetric radar. *Wea. Forecasting*, **28**, 139–158, doi:10.1175/WAF-D-11-00158.1.

Brown, J. M., and K. R. Knupp, 1980: The Iowa cyclonic–anticyclonic tornado pair and its parent thunderstorm. *Mon. Wea. Rev.*, **108**, 1626–1646, doi:10.1175/1520-0493(1980)108<1626:TICATP>2.0.CO;2.

——, and Coauthors, 2011: Improvement and testing of WRF physics options for application to Rapid Refresh and High Resolution Rapid Refresh. *14th Conf. on Mesoscale Processes/15th Conf. on Aviation, Range, and Aerospace Meteorology*, Los Angeles, CA, Amer. Meteor. Soc., 5.5. [Available online at https://ams.confex.com/ams/14Meso15ARAM/webprogram/Paper191234.html.]

Bunkers, M. J., and J. W. Stoppkotte, 2007: Documentation of a rare tornadic left-moving supercell. *Electron. J. Severe Storms Meteor.*, **2** (2). [Available online at http://www.ejssm.org/ojs/index.php/ejssm/article/viewArticle/14.]

Crum, T. D., and R. L. Alberty, 1993: The WSR-88D and the WSR-88D operational support facility. *Bull. Amer. Meteor. Soc.*, **74**, 1669–1687, doi:10.1175/1520-0477(1993)074<1669:TWATWO>2.0.CO;2.

Davies-Jones, R., D. Burgess, and M. Foster, 1990: Test of helicity as tornado forecast parameter. Preprints, *16th Conf. on Severe Local Storms*, Kananaskis Park, AB, Amer. Meteor. Soc., 588–592.

Doviak, R. J., and D. S. Zrnić, 1993: *Doppler Radar and Weather Observations*. 2nd ed. Academic Press, 562 pp.

Dowell, D. C., C. R. Alexander, J. M. Wurman, and L. J. Wicker, 2005: Centrifuging of hydrometeors and debris in tornadoes: Radar-reflectivity patterns and wind-measurement errors. *Mon. Wea. Rev.*, **133**, 1501–1524, doi:10.1175/MWR2934.1.

Edwards, R., 2014: Characteristics of supercellular satellite tornadoes. *27th Conf. on Severe Local Storms*, Madison, WI, Amer. Meteor. Soc., 17.5. [Available online at https://ams.confex.com/ams/27SLS/webprogram/Paper254326.html.]

French, M. M., 2012: Mobile, phased-array, Doppler radar observations of tornadoes at X-band. Ph.D. dissertation, University of Oklahoma, Norman, OK, 322 pp.

——, H. B. Bluestein, I. PopStefanija, C. Baldi, and R. T. Bluth, 2013: Reexamining the vertical development of tornadic vortex signature in supercells. *Mon. Wea. Rev.*, **141**, 4576–4601, doi:10.1175/MWR-D-12-00315.1.

——, ——, ——, ——, and ——, 2014: Mobile, phased-array, Doppler radar observations of tornadoes at X band. *Mon. Wea. Rev.*, **142**, 1010–1036, doi:10.1175/MWR-D-13-00101.1.

Fujita, T. T., 1963: *Analytical Mesometeorology: A Review. Meteor. Monogr.*, No. 27, Amer. Meteor. Soc., 125 pp.

——, 1981: Tornadoes and downbursts in the context of generalized planetary scales. *J. Atmos. Sci.*, **38**, 1511–1534, doi:10.1175/1520-0469(1981)038<1511:TADITC>2.0.CO;2.

——, and R. M. Wakimoto, 1982: Anticyclonic tornadoes in 1980 and 1981. Preprints, *12th Conf. on Severe Local Storms*, San Antonio, TX, Amer. Meteor. Soc., 9.R1, 401–404.

Golden, J. H., and D. Purcell, 1978: Life cycle of the Union City, Oklahoma, tornado and comparison with waterspouts. *Mon. Wea. Rev.*, **106**, 3–11, doi:10.1175/1520-0493(1978)106<0003:LCOTUC>2.0.CO;2.

Griffin, C. B., C. C. Weiss, A. E. Reinhart, J. C. Snyder, H. B. Bluestein, J. Wurman, K. A. Kosiba, and P. Robinson, 2015: In situ and radar observations of the low reflectivity ribbon. *37th Conf. on Radar Meteorology*, Norman, OK, Amer. Meteor. Soc., 4A.6. [Available online at https://ams.confex.com/ams/37RADAR/webprogram/Paper275417.html.]

Houser, J. L., H. B. Bluestein, and J. C. Snyder, 2015: Rapid-scan, polarimetric, Doppler-radar observations of tornadogenesis and tornado dissipation in a tornadic supercell: The "El Reno, Oklahoma" storm of 24 May 2011. *Mon. Wea. Rev.*, **143**, 2685–2710, doi:10.1175/MWR-D-14-00253.1.

Klemp, J. B., and R. Rotunno, 1983: A study of the tornadic region within a supercell thunderstorm. *J. Atmos. Sci.*, **40**, 359–377, doi:10.1175/1520-0469(1983)040<0359:ASOTTR>2.0.CO;2.

Knupp, K. R., and W. R. Cotton, 1982: An intense, quasi-steady thunderstorm over mountainous terrain. Part II: Doppler radar observations of the storm morphological structure. *J. Atmos. Sci.*, **39**, 343–358, doi:10.1175/1520-0469(1982)039<0343:AIQSTO>2.0.CO;2.

Kosiba, K. A., J. Wurman, Y. Richardson, P. Markowski, and P. Robinson, 2013: Genesis of the Goshen County, Wyoming, tornado on 5 June 2009 during VORTEX2. *Mon. Wea. Rev.*, **141**, 1157–1181, doi:10.1175/MWR-D-12-00056.1.

——, P. Robinson, P. W. Chan, and J. Wurman, 2014: Wind field of a nonmesocyclone anticyclonic tornado crossing the Hong Kong International Airport. *Adv. Meteor.*, **2014**, 597378, doi:10.1155/2014/597378.

Kramar, M. R., H. B. Bluestein, and A. L. Pazmany, 2005: The "Owl Horn" radar signature in developing Southern Plains supercells. *Mon. Wea. Rev.*, **133**, 2608–2634, doi:10.1175/MWR2992.1.

Lee, B. D., and R. B. Wilhelmson, 1997: The numerical simulation of nonsupercell tornadogenesis. Part I: Initiation and evolution of pretornadic misocyclone circulations along a dry outflow boundary. *J. Atmos. Sci.*, **54**, 32–60, doi:10.1175/1520-0469(1997)054<0032:TNSONS>2.0.CO;2.

——, C. A. Finley, and C. D. Karstens, 2012: The Bowdle, South Dakota, cyclic tornadic supercell of 22 May 2010: Surface analysis of rear-flank downdraft evolution and multiple internal surges. *Mon. Wea. Rev.*, **140**, 3419–3441, doi:10.1175/MWR-D-11-00351.1.

Lemon, L. R., 1976: Wake vortex structure and aerodynamic origin in severe thunderstorms. *J. Atmos. Sci.*, **33**, 678–685, doi:10.1175/1520-0469(1976)033<0678:WVSAAO>2.0.CO;2.

——, and C. A. Doswell III, 1979: Severe thunderstorm evolution and mesocyclone structure as related to tornadogenesis. *Mon. Wea. Rev.*, **107**, 1184–1197, doi:10.1175/1520-0493(1979)107<1184:STEAMS>2.0.CO;2.

Markowski, P. M., 2002: Hook echoes and rear-flank downdrafts: A review. *Mon. Wea. Rev.*, **130**, 852–876, doi:10.1175/1520-0493(2002)130<0852:HEARFD>2.0.CO;2.

——, and Y. P. Richardson, 2014: The influence of environmental low-level shear and cold pools on tornadogenesis: Insights from idealized simulations. *J. Atmos. Sci.*, **71**, 243–275, doi:10.1175/JAS-D-13-0159.1.

——, C. Hannon, J. Frame, E. Lancaster, A. Pietrycha, R. Edwards, and R. L. Thompson, 2003: Characteristics of vertical wind profiles near supercells obtained from the Rapid Update Cycle. *Wea. Forecasting*, **18**, 1262–1272, doi:10.1175/1520-0434(2003)018<1262:COVWPN>2.0.CO;2.

——, Y. Richardson, E. Rasmussen, J. Straka, R. Davies-Jones, and R. J. Trapp, 2008: Vortex lines within low-level mesocyclones obtained from pseudo-dual-Doppler radar observations. *Mon. Wea. Rev.*, **136**, 3513–3535, doi:10.1175/2008MWR2315.1.

Marquis, J., Y. Richardson, J. Wurman, and P. Markowski, 2008: Single- and dual-Doppler analysis of a tornadic vortex and

surrounding storm-scale flow in the Crowell, Texas, supercell of 30 April 2000. *Mon. Wea. Rev.*, **136**, 5017–5043, doi:10.1175/2008MWR2442.1.

Monteverdi, J. P., W. Blier, G. Stumpf, W. Pi, and K. Anderson, 2001: First WSR-88D documentation of an anticyclonic supercell with anticyclonic tornadoes: The Sunnyvale–Los Altos, California, tornadoes of 4 May 1998. *Mon. Wea. Rev.*, **129**, 2805–2814, doi:10.1175/1520-0493(2001)129<2805:FWDOAA>2.0.CO;2.

Nielsen-Gammon, J. W., and W. L. Read, 1995: Detection and interpretation of left-moving severe thunderstorms using the WSR-88D: A case study. *Wea. Forecasting*, **10**, 127–140, doi:10.1175/1520-0434(1995)010<0127:DAIOLM>2.0.CO;2.

Oye, R., C. Mueller, and S. Smith, 1995: Software for radar translation, visualization, editing, and interpolation. Preprints, *29th Conf. on Radar Meteorology*, Vail, CO, Amer. Meteor. Soc., 359–361.

Pazmany, A. L., J. B. Mead, H. B. Bluestein, J. C. Snyder, and J. B. Houser, 2013: A mobile, rapid-scanning, X-band, polarimetric (RaXPol) Doppler radar system. *J. Atmos. Oceanic Technol.*, **30**, 1398–1413, doi:10.1175/JTECH-D-12-00166.1.

Rotunno, R., 2013: The fluid dynamics of tornadoes. *Annu. Rev. Fluid Mech.*, **45**, 59–84, doi:10.1146/annurev-fluid-011212-140639.

——, and J. Klemp, 1985: On the rotation and propagation of simulated supercell thunderstorms. *J. Atmos. Sci.*, **42**, 271–292, doi:10.1175/1520-0469(1985)042<0271:OTRAPO>2.0.CO;2.

Ryzhkov, A. V., T. J. Schuur, D. W. Burgess, and D. S. Zrnić, 2005: Polarimetric tornado detection. *J. Appl. Meteor.*, **44**, 557–570, doi:10.1175/JAM2235.1.

Schultz, C. J., and Coauthors, 2012: Dual-polarization tornadic debris signatures Part II: Comparisons and caveats. *Electron. J. Oper. Meteor.*, **13** (10), 138–150.

Schiller, J., 2015: How a storm chaser captured a terrifying double tornado. *Wired*, 9 June 2015. [Available online at http://www.wired.com/2015/06/kelly-delay-double-tornado/.]

Skinner, P. S., C. C. Weiss, M. M. French, H. B. Bluestein, P. M. Markowski, and Y. P. Richardson, 2014: VORTEX2 observations of a low-level mesocyclone with multiple internal rear-flank downdraft momentum surges in the 18 May 2010 Dumas, Texas, supercell. *Mon. Wea. Rev.*, **142**, 2935–2960, doi:10.1175/MWR-D-13-00240.1.

Snyder, J. C., and H. B. Bluestein, 2014: Some considerations for the use of high-resolution mobile radar data in tornado intensity determination. *Wea. Forecasting*, **29**, 799–827, doi:10.1175/WAF-D-14-00026.1.

——, and A. V. Ryzhkov, 2015: Automated detection of polarimetric tornadic debris signatures. *J. Appl. Meteor. Climatol.*, **54**, 1861–1870, doi:10.1175/JAMC-D-15-0138.1.

——, H. B. Bluestein, and J. B. Houser, 2007: Doppler-radar analysis of a supercell that produced a cyclonic-anticyclonic pair of tornadoes in central Oklahoma. *33rd Conf. on Radar Meteorology*, Cairns, Queensland, Australia, Amer. Meteor. Soc., P13A.5. [Available online at https://ams.confex.com/ams/33Radar/webprogram/Paper122768.html.]

——, ——, G. Zhang, and S. Frasier, 2010: Attenuation correction and hydrometeor classification of high-resolution, X-band, dual-polarized mobile radar measurements in severe convective storms. *J. Atmos. Oceanic Technol.*, **27**, 1979–2001, doi:10.1175/2010JTECHA1356.1.

——, ——, V. Venkatesh, and S. J. Frasier, 2013: Observations of polarimetric signatures in supercells by an X-band mobile Doppler radar. *Mon. Wea. Rev.*, **141**, 3–29, doi:10.1175/MWR-D-12-00068.1.

——, J. L. Salazar-Cerreno, H. B. Bluestein, N. A. Aboserwal, R. D. Palmer, and T. Y. Yu, 2015: Examining the effects of

the ground on the radiation pattern of a parabolic reflector at very low elevation angles. *37th Conf. on Radar Meteorology*, Norman, OK, Amer. Meteor. Soc., 166. [Available online at https://ams.confex.com/ams/37RADAR/webprogram/Paper276116.html.]

Straka, J. M., E. N. Rasmussen, R. P. Davies-Jones, and P. M. Markowski, 2007: An observational and idealized numerical examination of low-level counter-rotating vortices in the rear flank of supercells. *Electron. J. Severe Storms Meteor.*, **2** (8). [Available online at http://www.meteo.psu.edu/~pmm116/pubs/2007/SRDM07EJSSM.pdf.]

Tanamachi, R., H. B. Bluestein, J. B. Houser, S. J. Frasier, and K. M. Hardwick, 2012: Mobile, X-band, polarimetric Doppler radar observations of the 4 May 2007 Greensburg, Kansas, tornadic supercell. *Mon. Wea. Rev.*, **140**, 2103–2125, doi:10.1175/MWR-D-11-00142.1.

Thompson, R. L., R. Edwards, J. A. Hart, K. L. Elmore, and P. Markowski, 2003: Close proximity soundings within supercell environments obtained from the Rapid Update Cycle. *Wea. Forecasting*, **18**, 1243–1261, doi:10.1175/1520-0434(2003)018<1243:CPSWSE>2.0.CO;2.

Trapp, R. J., E. D. Mitchell, G. A. Tipton, D. W. Effertz, A. I. Watson, D. L. Andra, and M. A. Magsig, 1999: Descending and nondescending tornadic vortex signatures detected by WSR-88Ds. *Wea. Forecasting*, **14**, 625–639, doi:10.1175/1520-0434(1999)014<0625:DANTVS>2.0.CO;2.

Vasiloff, S. V., 2001: Improving tornado warnings with the Federal Aviation Administration's Terminal Doppler Weather Radar. *Bull. Amer. Meteor. Soc.*, **82**, 861–874, doi:10.1175/1520-0477(2001)082<0861:ITWWTF>2.3.CO;2.

Wakimoto, R. M., and J. W. Wilson, 1989: Non-supercell tornadoes. *Mon. Wea. Rev.*, **117**, 1113–1140, doi:10.1175/1520-0493(1989)117<1113:NST>2.0.CO;2.

——, and B. E. Martner, 1992: Observations of a Colorado tornado. Part II: Combined photogrammetric and Doppler radar analysis. *Mon. Wea. Rev.*, **120**, 522–543, doi:10.1175/1520-0493(1992)120<0522:OOACTP>2.0.CO;2.

——, N. T. Atkins, and J. Wurman, 2011: The LaGrange tornado during VORTEX2. Part I: Photogrammetric analysis of the tornado combined with single-Doppler radar data. *Mon. Wea. Rev.*, **139**, 2233–2258, doi:10.1175/2010MWR3568.1.

——, P. Stauffer, W.-C. Lee, N. T. Atkins, and J. Wurman, 2012: Finescale structure of the LaGrange, Wyoming, tornado during VORTEX2: GBVTD and photogrammetric analyses. *Mon. Wea. Rev.*, **140**, 3397–3418, doi:10.1175/MWR-D-12-00036.1.

——, N. T. Atkins, K. M. Butler, H. B. Bluestein, K. Thiem, J. Snyder, and J. Houser, 2015: Photogrammetric analysis of the 2013 El Reno tornado combined with mobile X-band polarimetric radar data. *Mon. Wea. Rev.*, **143**, 2657–2683, doi:10.1175/MWR-D-15-0034.1.

Weisman, M. L., 1992: The role convectively generated rear-inflow jets in the evolution of the long-lived mesoconvective systems. *J. Atmos. Sci.*, **49**, 1826–1847, doi:10.1175/1520-0469(1992)049<1826:TROCGR>2.0.CO;2.

——, 1993: The genesis of severe, long-lived bow echoes. *J. Atmos. Sci.*, **50**, 645–670, doi:10.1175/1520-0469(1993)050<0645:TGOSLL>2.0.CO;2.

——, and C. A. Davis, 1998: Mechanisms for the generation of mesoscale vortices within quasi-linear convective systems. *J. Atmos. Sci.*, **55**, 2603–2622, doi:10.1175/1520-0469(1998)055<2603:MFTGOM>2.0.CO;2.

Wood, V. T., and R. A. Brown, 1997: Effects of radar sampling on single-Doppler velocity signatures of mesocyclones and

tornadoes. *Wea. Forecasting*, **12**, 928–938, doi:10.1175/1520-0434(1997)012<0928:EORSOS>2.0.CO;2.

Wurman, J., and S. Gill, 2000: Finescale radar observations of the Dimmitt, Texas (2 June 1995), tornado. *Mon. Wea. Rev.*, **128**, 2135–2164, doi:10.1175/1520-0493(2000)128<2135:FROOTD>2.0.CO;2.

——, and K. Kosiba, 2013: Finescale radar observations of tornado and mesocyclone structures. *Wea. Forecasting*, **28**, 1157–1174, doi:10.1175/WAF-D-12-00127.1.

——, J. M. Straka, E. N. Rasmussen, M. Randall, and A. Zahrai, 1997: Design and deployment of a portable, pencil-beam, pulsed, 3-cm Doppler radar. *J. Atmos. Oceanic Technol.*, **14**, 1502–1512, doi:10.1175/1520-0426(1997)014<1502:DADOAP>2.0.CO;2.

——, Y. Richardson, C. Alexander, S. Weygandt, and P. F. Zhang, 2007: Dual-Doppler and single-Doppler analysis of a tornadic storm undergoing mergers and repeated tornadogenesis. *Mon. Wea. Rev.*, **135**, 736–758, doi:10.1175/MWR3276.1.

——, D. Dowell, Y. Richardson, P. Markowski, E. Rasmussen, D. Burgess, L. Wicker, and H. B. Bluestein, 2012: The Second Verification of the Origin of Rotation in Tornadoes Experiment. *Bull. Amer. Meteor. Soc.*, **93**, 1147–1170, doi:10.1175/BAMS-D-11-00010.1.

——, K. Kosiba, P. Robinson, and T. Marshall, 2014: The role of multiple-vortex tornado structure in causing storm researcher fatalities. *Bull. Amer. Meteor. Soc.*, **95**, 31–45, doi:10.1175/BAMS-D-13-00221.1.